PARTICLE ASSISTED CHEMICAL VAPOR DEPOSITION OF DIAMOND USING AN ELECTRON CYCLOTRON RESONANCE ENHANCED PLASMA SYSTEM

By

DONALD R. GILBERT

A DISSERTATION PRESENTED TO THE GRADUATE SCHOOL
OF THE UNIVERSITY OF FLORIDA IN PARTIAL FULFILLMENT
OF THE REQUIREMENTS FOR THE DEGREE OF
DOCTOR OF PHILOSOPHY

UNIVERSITY OF FLORIDA

1998

ACKNOWLEDGMENTS

I would like to express my gratitude to all those who have contributed to my attainment of this life goal. I would like to thank my advisory chair, Dr. Rajiv Singh, for his many years of support and guidance in this process. Also, I must express my sincere appreciation to my other advisory committee members, Dr. Holloway, Dr. DeHoff, Dr. Adair (who was unable to see me entirely through my degree due to career opportunities outside UF), Dr. Abernathy (who graciously agreed to fill in the vacancy late in my graduate career), and Dr. Shah of the Chemical Engineering department. I must acknowledge the valuable contributions of Sherry Staehle, Melanie Carasso, and Paul Demkowicz for their critical roles in the development of the novel particle seeding process utilized in this work. I must also acknowledge the assistance of Sanju Gupta and Ming Huang in providing critical Raman characterization. Also, I would like to acknowledge the support of the Engineering Research Center for Particle Science and Technology.

In the course of my work here, I have met many interesting people who have rarely failed to surprise me in their generous expressions of support and friendship. It would be impractical to attempt to mention each and every one of these people here, but it is my hope that they know who they are and how much I appreciate what they have given me. Among those many, I must mention a few individuals who have particularly touched my life in these years of discovery. First, I must acknowledge Dr. Robert Linares, who started me on this academic journey and provided critical encouragement along the way. To John Viatella, I owe great thanks for years of close friendship. Also, I offer my sincere gratitude to Lani Kirk, for her constant support and sympathetic ear. To Karen, Brock, Brent, Dong-gu, Fan, Rich, Jim, and all my other friends, I thank you for all the help and the good times we have shared, which have made these some of the best, if not the easiest, years of my life.

Finally, and most especially, I must thank my family for their unwavering support, both emotional and financial, over my entire lifetime leading to the culmination of this endeavor, without which this truly would not have been possible.

TABLE OF CONTENTS

ACKNOWLEDGMENTS ii

ABSTRACT vi

1. INTRODUCTION AND MOTIVATION 1

2. BACKGROUND AND LITERATURE REVIEW 4

- Diamond Structure and Properties 4
- Diamond Synthesis 7
  - High Temperature, High Pressure 7
  - Chemical Vapor Deposition 7
    - Nucleation and growth 10
      - Nucleation enhancement 11
      - Texturing and growth direction . . . 14
    - Substrate materials 17
  - Deposition Systems 19
    - Hot-filament 19
    - Plasma enhancement 21
    - Torch 23
- Electron Cyclotron Resonance 24
  - ECR CVD of Diamond 26

3. EXPERIMENTAL SETUP AND PROCEDURES 46

- Diamond Deposition 46
  - System Design 46
  - Sample Preparation 49
    - Particle abrasion 49
    - Electrophoretic seeding 49
    - Electrostatic seeding 50
  - Deposition Procedure 52
- Characterization 53
  - Microscopy 53
    - Scanning electron microscopy 54
    - Atomic force microscopy 54
  - Micro-Raman Spectroscopy 55

Background 55
Sample characterization 58
Optical Emission Spectroscopy 60

4. RESULTS AND DISCUSSION 80

Early Experiments 80
Current Work 82
Pressure Variation 83
Temperature Variation 88
Power Variation 90
Gas Composition Variation 93
Variable Seed Densities 98
Discussion of Results 108
General Deposition Characteristics 108
Film Stress 114
Microstructural Control 119

5. CONCLUSIONS 175

System Dependent Deposition Conditions 175
Controlled Areal Seeding 177

LIST OF REFERENCES 178

BIOGRAPHICAL SKETCH 186

Abstract of Dissertation Presented to the Graduate School
of the University of Florida in Partial Fulfillment of the
Requirements for the Degree of Doctor of Philosophy

PARTICLE ASSISTED CHEMICAL VAPOR DEPOSITION OF DIAMOND USING AN ELECTRON CYCLOTRON RESONANCE ENHANCED PLASMA SYSTEM

By

Donald R. Gilbert

August 1998

Chairperson: Rajiv K. Singh
Major Department: Materials Science and Engineering

Lowering the deposition pressure of diamond from the vapor phase has significant potential technological benefit in terms of facilitating more uniform, larger area coatings grown at lower temperatures than is possible in present standard deposition systems. The objective of this research was to investigate deposition of diamond films at pressures below 2.0 Torr at relatively low substrate temperatures. Diamond films were deposited from methyl alcohol vapor and hydrogen gas mixtures using an electron cyclotron resonance enhanced microwave plasma system. Plasma system parameters of gas pressure, substrate temperature, microwave power, and gas composition were varied and the resultant deposits were characterized with regard to morphology and structural characteristics using scanning electron microscopy, atomic force microscopy, and micro-Raman spectroscopy. Optical emission spectroscopy was used to investigate the behavior of the plasma system and draw correlations between gas related system parameter variations and resultant deposition characteristics.

It was found that the primary effects of pressure, power, and gas composition were related to the alteration of the resultant composition of the plasma through gas phase reactions. Alterations in the relative concentrations of atomic hydrogen and oxygen species, as well as the formation of CH radicals and carbon dimers and trimers, resulted in significant variations in film properties of phase purity, crystal quality, and relative growth rates. Substrate temperatures showed more limited effects, primarily relating to the phase purity and preferred crystallographic growth direction for the conditions investigated.

Diamond-particle seeding of substrates was necessary for the consistent formation of continuous coatings under the conditions investigated. A novel seeding process was developed and used to provide samples of uniform nucleation characteristics. Use of controlled areal particle densities was investigated to determine the sensitivity of resultant film characteristics to nucleation density. Particle density most affected film microstructure, determining initial average lateral grain size upon film coalescence and resultant surface roughness, although seed particle size non-uniformity caused variation from theoretically predicted results. Phase purity and intrinsic stress showed relatively little dependence on areal seed density, most likely due to impurity inclusion in the grain boundaries.

CHAPTER 1
INTRODUCTION AND MOTIVATION

A great deal of interest and excitement was generated in the scientific community with the advent of diamond chemical vapor deposition. Diamond's many superlative properties, such as extremely high hardness and thermal conductivity, make it a very attractive material for a wide variety of applications. Although production of high quality diamond in substantial bulk form remains outside current process capabilities, its usefulness as a thin film coating material has driven a significant world-wide research effort. Many different types of deposition technologies have been investigated, each with its own potential niche for diamond film formation, such as high growth rate, large area, high crystal quality, low temperature, homoepitaxial, or textured (near-heteroepitaxial) polycrystalline deposition. Diamond's potential applications include: wear-resistant coatings for cutting-tools and infrared optics, heat spreading for thermal management of microelectronics, low-friction hard coatings for sliding contacts, fabrication of high-temperature microelectronic devices, and cold cathode emitters for flat-panel displays.

The lowering of deposition temperatures and pressures has several potential technological benefits to the practical application of diamond coatings. Most generally, lowering of the deposition temperature can allow a wider range of possible substrate materials, specifically those with relatively low melting temperatures. Stresses generated by differences in the thermal expansion rates of coated materials and the diamond coating can cause structural failure of the film through cracking and delamination. Lowering of the deposition temperature generally results in a reduction of thermal expansion difference between the film and substrate and hence a reduction of the resultant stress. Lowering of the gas pressure used for deposition can actually have a direct impact in lowering the resultant gas temperature in a plasma system, which in turn may facilitate the lowering of the substrate temperature without the need for active substrate cooling. Also, lower gas pressure environments have inherently larger diffusion lengths that tend to facilitate deposition of uniform diamond films over relatively large areas, which is also a necessary pursuit for the application of diamond coatings. However, at the same time that deposition temperatures and pressures are lowered, difficulties arise in the initiation (i.e., nucleation) of diamond growth on non-diamond substrates. The most effective method to avoid this problem is to put diamond particles down on the proposed substrate surface as "seeds" for growth in sufficient quantities to facilitate the rapid formation of a continuous film. At the same time particle seeding of the substrate can aid in film formation, it may significantly influence the characteristics and properties of the resultant film. Therefore, careful control of the seeding process and an understanding of its influence on resultant films is highly desirable.

The objective of this research was to investigate the diamond deposition behavior of a custom ECR plasma system at relatively low deposition pressures and substrate temperatures. In conjunction with this system, a novel technique for the formation of diamond particle seed layers with controlled areal density characteristics was investigated. The relevance of this research has been illustrated in the formation of an adherent diamond film on sapphire (a highly problematic material due to its high thermal expansion coefficient [May94]) through the combined use of both the low temperature deposition capabilities of the ECR system and seeding of the sapphire surface [Sin96a].

CHAPTER 2
BACKGROUND AND LITERATURE REVIEW

Diamond Structure and Properties

Diamond is a carbon allotrope, bonded tetrahedrally in the diamond-cubic lattice structure (two interpenetrating face-centered cubic lattices with a displacement of 1/4 body diagonal) as the result of sp^3 orbital hybridization. Figure 2.1 shows the diamond cubic lattice unit cell. This bond structure, in combination with carbon's low atomic number, gives diamond the highest atom density of any material, which in turn is responsible for many of diamond's superlative properties. Table 2.1 provides a brief listing of physical properties for diamond along with corresponding silicon values for comparison. The clean, unreconstructed diamond surface exhibits very high surface energy values. However, diamond is typically terminated by impurity species at its surface. This surface termination, commonly hydrogen and oxygen, acts to reduce the surface energy.

Diamond is a semi-insulating material possessing a bandgap with a minimum value of 5.45 eV. Like silicon, it is an indirect bandgap material with the minimum of the

Table 2.1 Physical Properties of Diamond and Silicon

PROPERTY	Diamond	Silicon
Lattice Constant (Å)	3.567	5.430
Density ($g \cdot cm^{-3}$)	3.515	2.328
Atomic Mass ($g \cdot mol^{-1}$)	12.011	28.0855
Hardness ($kg \cdot mm^{-2}$)	~10^4	10^3
Young's Modulus (GPa)	10.5×10^3	1.13×10^3
Sound Velocity (m/s)	18000	7500
Poisson's Ratio	0.07*	0.223
Bandgap (eV)	5.45	1.1
Resistivity ($\Omega \cdot cm$)	$>10^{15}$	10^3
Electron Mobility ($cm^2 \cdot V^{-1} \cdot s^{-1}$)	2200	1500
Hole Mobility ($cm^2 \cdot V^{-1} \cdot s^{-1}$)	1600	480
Dielectric Constant	5.7	11.8
Thermal Conductivity ($W \cdot cm^{-1} \cdot K^{-1}$)	20.0	1.47
Molar Heat Capacity, $c_{p,\ 298\ K}$ ($J \cdot mol^{-1} \cdot K^{-1}$)	6.19	19.85
Debye Temperature, Θ_D (K)	1860 ± 10	650

* isotropic aggregate value; $\nu_{21} = 0.104$

conduction band offset from the maximum of the valence band. In its intrinsic state, diamond exhibits extremely high resistivity, with measured values of greater than 10^{15} $\Omega \cdot cm$. As a result of its wide bandgap nature, the diamond surface shows negative electron affinity (NEA) characteristics. This means that the conduction band minimum energy lies above the vacuum level, providing no potential barrier to electron emission from the diamond surface. A schematic of an ideal NEA energy band configuration is shown in Figure 2.2. The exact nature of the electron affinity characteristics of diamond is sensitive to both crystallographic orientation and surface impurity termination. Diamond typically shows a hydrogen termination layer at its surface, and may also form a high degree of oxygen termination, depending on the process environment. A hydrogen terminated diamond surface will exhibit NEA, whereas oxygen termination reduces or eliminates NEA behavior.

Optically, diamond is highly transmitting over a very wide spectral range. It exhibits a near-ultraviolet (bandgap) cut-off at 226.5 nm and transmits into the far infrared. Depending on the impurity characteristics of the material, there may be several near-IR absorption peaks in the spectral region of 2 to 12 µm. There is a characteristic diamond two-phonon absorption peak in the region from 1333 - 2666 cm^{-1}. Diamond has an Abbe number ($(n_{589.29}-1)/(n_{486.13}-n_{654.28})$, n=index of refraction) of 55.3 ($n_{589.29}=2.4173$, $n_{486.13}=2.4355$, and $n_{654.28}=2.4099$). The Abbe number represents a measure of the optical dispersion characteristics of a material over the visible spectral range. It is used in the evaluation of materials in lens systems, where it has direct bearing on the amount of chromatic aberration observed. For comparison, fused silica and BK-7 (borosilicate) glasses have Abbe numbers of 67.8 and 64.2, respectively, while high refractive index plastics have Abbe numbers between 30 and 40. Higher Abbe values indicate less distortion in lens applications.

Diamond Synthesis

High Temperature, High Pressure

The desire to manufacture diamond has existed since it was first determined to be a form of carbon around the turn of the 19th century. Repeatable high pressure, high temperature (HPHT) production of diamond was first demonstrated in 1955 by researchers at General Electric [Nas93]. High pressure techniques have been used for the production of synthetic diamonds and diamond grit ever since. Formation of diamond at standard thermodynamic equilibrium occurs at pressures greater than 100,000 atmospheres and temperatures of 1000 °C or more. Molten metal catalysts are generally used to reduce these required temperatures and pressures. Diamond grit so produced is commonly used in grinding, polishing, and cutting applications. These applications typically involve incorporation of the diamond particles in a metallic binder to produce the desired shape.

Chemical Vapor Deposition

Chemical vapor deposition of diamond represents a radical departure from the standard HPHT process. Diamond CVD covers a broad range of possible system pressures, from the millitorr range up to atmospheric pressure, and substrate temperatures, reportedly as low as 200 °C to greater than 1000 °C [Mur94, Bac91]. However, there are certain factors that are common to all diamond CVD processes. First and foremost is the requirement for a gaseous carbon source, typically in the form of a monomer such as methane (CH_4), acetylene (C_2H_2), carbon monoxide (CO), or methyl alcohol (CH_3OH). Also critical to diamond CVD is the presence of a diluent gas, usually hydrogen. There is also the necessity of an energetic activation source, such as a hot filament or an electric field, to dissociate some of the hydrogen and to produce appropriate growth species, typically the methyl radical (CH_3). Finally, some material must be present upon which diamond may form under the given process conditions. Substrate temperature primarily affects the structural quality of the deposited material and the rate of deposition.

If a ternary compositional diagram of the process gas is drawn consisting of carbon, oxygen and hydrogen, (the primary elemental components in most diamond CVD systems) the generally observed possible atomic fraction compositions for depositing diamond fall in a roughly triangular region about the CO line. This was first determined in a survey conducted of the reported compositions of successful diamond formation from a wide range of researchers, and became known as the Bachmann triangle [Bac91]. Figure 2.3 shows a schematic approximation of this region. Vital to the interpretation of this figure is the understanding that gas activation must be sufficient to neglect the original bonding character of the source gases. Source monomers must be sufficiently dissociated to form active growth species (radicals), some amount of atomic hydrogen must be produced, and, if present, molecular oxygen must dissociate and react sufficiently with the other species to play its role in the growth process effectively. Implicit in this statement is the effect of gas pressure on the activation process: changes in gaseous diffusion lengths, interaction cross sections and transient species lifetimes will accordingly affect the outcome of the deposition process. Also, the relative structural quality of the resulting deposition, in terms of defects and non-diamond inclusions, may vary greatly within this compositional region of "possible" diamond deposition [Ang95].

A great deal of effort has been put into developing theories and models for the mechanisms by which diamond CVD occurs [Bac91, Bar89, Fre91, Chu90, Pie89, Meh90]. Diamond deposition can proceed from many different monomers. The methyl radical, CH_3, is the most efficient growth monomer for most systems [Har94, Dev92]. Hydrogen plays several important roles in the deposition process [Fre89, Mur90]. As carbon is deposited on the pre-existing material, the diamond crystal structure is stabilized through hydrogen termination of the surface. Graphitic phase or highly defective sp^3 material is etched by atomic hydrogen at a higher rate than diamond phase carbon. Abstraction of surface terminating hydrogen occurs through interaction with impinging atomic hydrogen, which subsequently leaves active sites available for carbon addition. The role of oxygen in diamond deposition is similar in many ways to that of hydrogen [Bel91]. Oxygen is a more efficient carbon etchant than hydrogen. Like hydrogen, oxygen may adsorb onto and partially terminate the diamond surface. Another role of oxygen in the growth process is to combine with gas phase carbon as carbon monoxide, which is extremely stable. This may effectively remove "excess" hydrocarbons from the deposition reaction, improving the quality of the deposited material [Pin93].

Nucleation and growth

Two critical facets that must be considered in diamond CVD, as with many thin-film CVD processes, are the processes of nucleation and growth. Both aspects play critical roles in the resulting characteristics of the deposited film. The density of nuclei, which is primarily determined by nucleation rate, has significant influence on initial lateral grain size and can substantially affect as-grown surface roughness. Growth rate, particularly as it pertains to crystallographic direction, can also play a critical role in determining resulting film properties such as surface roughness and defect density [Ang95]. Both nucleation rates and growth rates are influenced by temperature, gas chemistry, and gas activation. Nucleation may be particularly sensitive to the choice of substrate material, as well [Wei92, Par91, Nar92, Xi194].

Regarding diamond CVD growth rates, higher gas phase temperatures generally correlate with faster deposition rates. This is observed in the high deposition rates of torch CVD systems. In plasma-based systems, higher growth rates are observed at higher plasma densities. DC arc jets have achieved some of the highest diamond deposition rates to date.

Nucleation enhancement

Homogeneous nucleation of diamond on untreated, non-diamond materials is an energetically unfavorable process. Initial nucleation on untreated surfaces tends to occur at defect sites and can result in discontinuous coverage and non-uniform film characteristics. This process can be enhanced by abrading the substrate surface with diamond grit, usually by means of exposure to a diamond colloid (particle sizes from 0.25 - 100 µm, typically) in an ultrasonic bath [Ram92, Fay94]. This provides two possible enhancement mechanisms:

first, the surface is thoroughly scratched, providing a high density of surface defect sites; second, microcleavage of the impinging particles leaves nanometer sized diamond remnants imbedded in the surface that may act as nucleation "seeds" for diamond growth [Yan96]. Such abrasion has been shown to provide nucleation densities as high as 10^{10} cm^{-2} in a microwave plasma CVD system. Observed nucleation densities following diamond abrasion are inherently influenced by the deposition process conditions [Fay94, Kim92]. Low temperature deposition will show inherently lower nucleation rates than deposition at higher substrate temperatures. Nucleation rate may also change as a function of surface coverage by previously formed diamond nuclei during the early stages of CVD [Sti96].

One drawback of the abrasion method for enhancing diamond nucleation is that the substrate surface is being damaged, which is undesirable for applications such as optical coatings. A common method of enhancing diamond nucleation in such cases is through the controlled seeding of the growth surface with diamond particles [Val91, Yan95, Car97, Mak96]. In fact, this functionally avoids the nucleation process because there is no real barrier to growth of the seed particles once the deposition environment is established. Particle seeding is also useful for low temperature deposition processes where abrasion would be of limited benefit [Yar95].

Diamond particles may be delivered in a colloid to the substrate surface by several means, depending on the suspending medium and the substrate surface characteristics. Various delivery methods for colloid-based seeding include spraying, spin-coating, brush painting, direct writing and dipping [Yan95, Car97, Mak96]. More reliable seed coatings with better particle adhesion characteristics can be obtained using an intermediate monolayer coating of polymer that may provide an electrostatically favorable surface relative to the colloidal particle surface charge [Ste94, Car97]. Electrophoretic deposition, which involves the application of a bias potential to the substrate of opposite polarity to the intrinsic surface charge of the colloidal diamond particles, has also been used to seed conducting and semiconducting substrates [Val91, Lee97]. If seed layers can be imparted at predetermined areal densities, they can be used to control the microstructural characteristics of the diamond film, primarily in regard to lateral grain size upon film coalescence. The use of nanometer-sized particles can allow very high nucleation densities ($\leq 10^{11}$ cm^{-2}) to be achieved [Mak96, Yar95]. Such high nucleation densities allow the formation of very thin (< 0.1 μm) continuous films with concomitantly low surface roughness [Yan95, Mak96]. Also, if seeding can be controlled lithographically, where specific patterns can either be covered or be left bare at the micron scale, then microelectronic and micromechanical applications are facilitated [Val91, Mas91]. Figure 2.4 shows examples of lithographically defined features formed using the novel electrostatic-controlled seeding process (detailed in Chapter 3) and subsequent deposition.

Perhaps one of the most encouraging developments in diamond CVD is the bias-enhanced nucleation (BEN) process [Yug91, Ger94, Che95, Rei95]. In this procedure, a negative bias voltage is applied to the substrate during the nucleation stage of deposition. Resulting bombardment of ionic species causes the formation of a thin carbide layer (epitaxial β-SiC for silicon under the proper conditions) on the substrate surface [Ger94, Che95, Rei95]. In addition to carbide formation, biasing also enhances the diamond nucleation rate, in part through the rapid formation of amorphous carbon on the substrate surface, thus facilitating continuous film coverage.

Texturing and growth direction

If proper process conditions are used, the resultant nuclei that form during bias-enhanced nucleation on single crystal substrates are highly oriented with respect to the substrate and hence to each other, thus forming a near-epitaxial film, typically referred to as highly oriented diamond (HOD) [Rei95, Wil93]. These films have been characterized by low angle grain boundaries with misorientations of ~4°. Electrical and thermal characteristics of such films can be expected to be substantially improved over those of otherwise comparable (i.e., grain size, film thickness, impurity/defect structure, etc.) non-oriented polycrystalline films [Sto93].

Alternatively, HOD films have also been produced without the use of electrical biasing. Imparting diamond particles onto nickel substrates with subsequent heat treating can produce highly oriented nuclei [Yan94]. Successive deposition leads to HOD formation, with corresponding low angle grain boundaries and improved thermal and electrical characteristics.

Another method of producing preferentially oriented nuclei has been demonstrated through electrophoretic seeding [Lee97]. Using a colloid of 5 μm average sized diamond particles, the electrophoretic process can produce a seed layer with a statistically preferred (≥80%) orientation toward the ⟨111⟩ direction. This phenomenon has been observed for seeding at or below one monolayer coverage of the substrate surface.

This leads to another important topic of interest, namely texture formation in typical polycrystalline diamond films. As mentioned above, the BEN process can produce HOD films that form in a nearly epitaxial (highly textured) state. However, any polycrystalline diamond film exhibiting columnar grain growth will develop threading texture characteristics under constant growth conditions if deposited to sufficiently large thicknesses. This is the result of the competition between grains having different crystallographic orientation with respect to the growth surface, based on the direction of fastest growth for the deposited diamond. Van der Drift first described this process, known as evolutionary selection, in which grains whose fastest growth direction is best aligned with the film surface-normal overgrow adjacent grains that are not so aligned [Van67]. As processing conditions of substrate temperature and gas composition are varied, different crystallographic directions will exhibit higher growth rates. Typically, this is characterized by a term known as the growth parameter, α, which is proportional to the ratio of the growth velocity in the $\langle 100 \rangle$ direction to the growth velocity in the $\langle 111 \rangle$ direction:

$$\alpha = \sqrt{3} \cdot \frac{\vec{V}_{\langle 100 \rangle}}{\vec{V}_{\langle 111 \rangle}}$$

[Bar94, Wil93, Bai92]. As a result, the growth parameter for regular crystals covers a range $1 \leq \alpha \leq 3$, with the former value signifying a cubic grain structure and the latter an octahedral shape. Figure 2.5 shows several examples of ideal regular crystal forms in the evolution from cubic to octahedral crystal forms along with corresponding approximate growth parameter values.

Substrate materials

Thus far, we have discussed fundamental issues of nucleation and growth without much consideration of the substrate material. However, this is another prime concern in diamond CVD. While diamond may be formed on a fairly wide range of materials, it will not necessarily remain intact upon removal from the growth system. Due to diamond's low thermal expansion coefficient and high modulus, as well as the rigors of the deposition environment, the range of suitable substrate materials is somewhat limited. Film adhesion is a critical consideration in diamond growth. Poor matching of thermal expansion characteristics over the process temperature range can result in excessively large thermally-induced residual stresses that can cause structural failure. Formation of a thin carbide layer at the substrate surface can greatly aid in film adhesion strength via chemical bonding. Also, adhesion may be improved through controlled roughening of the substrate surface for applications that will allow such an interface [Sin96b]. Microroughened surfaces provide increased interfacial area as well as an element of mechanical interlocking.

The majority of work done on CVD diamond has involved polycrystalline films deposited on non-diamond substrates. This is primarily due to the lack of suitable, readily available large-area substrates for epitaxial growth. Available diamond single crystals, both natural and synthetic, are relatively small and of variable quality, as well as being relatively expensive. Cubic boron nitride (c-BN), which is the most similar material to diamond and hence the most likely candidate material for heteroepitaxial diamond deposition, also shares diamond's limitations of problematic fabrication and is not available in large single crystals. Other materials that may provide reasonable low-index-plane lattice matching, such as copper or nickel, have other materials problems of large thermal-expansion mismatch, high carbon solubility/diffusivity and lack of stable carbide formation. As a result, epitaxial growth investigation has been more limited in scope than polycrystalline growth.

Candidate materials for diamond deposition must withstand the deposition environment with minimal effects. This implies insensitivity to atomic hydrogen exposure at growth temperature, phase/structure stability at temperatures of at least 500 °C (more typically up to ~ 700 - 800 °C or higher), and low vapor pressure at growth temperature. Materials such as ZnS and GaAs will generally not meet these requirements without some kind of encapsulating interlayer. As well as standing up to the growth environment, the substrate should not exhibit too high a solubility/diffusivity for carbon, as happens with iron. This can prevent effective nucleation due to the rapid absorption of diamond nuclei. Such materials will require a low-diffusivity interlayer for effective film formation [Tel95]. All of the above considerations have resulted in silicon being the most widely used substrate in diamond CVD research, i.e., low thermal expansion mismatch, stable carbide formation, low vapor pressure, etc. Refractory metals such as tungsten and molybdenum have also been used extensively as substrates, although they are less ideal materials due to their higher thermal expansion values and carbon diffusivity.

Deposition Systems

As previously mentioned, there are many systems that can be used for the deposition of diamond. These systems cover a wide range of process pressures and temperatures, with corresponding variations in deposition rates and material qualities.

Hot-filament

The earliest work in diamond chemical vapor deposition was done using a thermal gas-activation process [Eve62, Ang68]. This basic type of system, utilizing a hot filament

(HF-CVD), has been extensively used and explored over the years, establishing it as the most fundamental of all diamond CVD systems. A refractory metal filament (such as W or Ta) is resistively heated to temperatures of 2000 - 2200 °C, sufficient to thermally dissociate hydrogen, in a vacuum chamber at typical operating pressures of 20 - 100 Torr. Substrates are typically placed within two centimeters of the filament, where they may be independently heated/cooled or they may be heated by the filament. Growth rates may run up to several microns per hour, depending on the conditions used. While the potential deposition area for an individual element is limited to a few centimeters, properly configured arrays of filaments may allow deposition over very large areas.

Carbon incorporation, or carburization, of the filament under these conditions is inevitable. In tungsten, this carburization results in significant embrittlement of the filament, requiring care in handling to maximize the lifetime of the unit. Rhenium filaments experience less embrittlement than tungsten, but do exhibit swelling because of carbon incorporation. Also, there is a significant change in the resistivity of the filament during the carburization process. Common practice when a new filament is installed in a reactor is to allow the filament to fully carburize before attempting film deposition, in order to maintain consistent conditions.

This may be determined through simple observation of the change in resistance of the filament over time, where "saturation" corresponds to steady state resistance. The time required for full carburization depends on the radius of the filament and the temperature of operation. HF-CVD diamond typically exhibits metal impurities originating from the filament. Oxygen addition to the process gas in the hot-filament system can cause degradation of the filament due to oxidation.

The hot-filament CVD system has the advantage of simple basic design and concomitantly low cost. It requires only a single stage pumping system and modest chamber materials requirements. A quartz enclosure (either a belljar or a capped cylinder) is common for small systems, facilitating visual process observation. Filament temperature is commonly monitored with an optical pyrometer. A diagram of a simple hot-filament system is shown in Figure 2.6.

Plasma enhancement

Plasma-enhanced (PE-CVD) deposition of diamond has been demonstrated using a wide range of excitation sources, including DC, RF, and microwave [Bac91, Nak90, Ree93, Oht90, Wat92, Shi92a, Rud92, Wat88, Ama89, Cha88, Gru94, Edd93, Sin92]. These systems provide various possible advantages over the thermal deposition process, from lower possible deposition temperatures and reduced metal impurity incorporation (especially for electrodeless systems) to greatly enhanced growth rates and novel gas chemistries.

As previously mentioned, diamond deposition rates for plasma-based systems generally correlate directly with the plasma density. DC plasma jet/torch systems have reported high deposition rates approaching 1 mm/hr, but are more commonly operated at growth rate conditions of a few microns per hour [Oht90]. However, DC plasma torch systems generally offer relatively small deposition areas with large growth non-uniformity.

Microwave plasma based systems may be the most common type of diamond deposition system next to the hot-filament type [Wat88, Ama89, Cha88]. Systems designed specifically for diamond deposition are commercially available and typically operate over the same pressure range as hot filament systems (~10 - 100 Torr). Deposition rates in these systems are typically several microns per hour using common hydrogen-based compositions. Work has also been done using microwave PE-CVD with an argon ambient and fullerenes (C_{60}) as the source chemistry for diamond deposition [Gru94]. This compositional system exploits the role of the carbon dimer (C_2), which is formed through fragmentation of the C_{60} structure, as a diamond growth precursor, in contrast to the methyl radical mentioned previously. By avoiding the presence of large amounts of atomic hydrogen in the system, it may be possible to expand the list of viable substrate materials as well as reducing the amount of incorporated hydrogen in the deposited material.

Torch

Possibly the simplest of all diamond deposition systems is the oxy-acetylene torch. This system operates at atmospheric pressure with very high growth rates (up to hundreds of microns per hour). Samples must be cooled during deposition to prevent substrate and film degradation. However, despite the high deposition rate, the torch system is very inefficient, consuming large amounts of fuel during deposition and having a relatively small effective deposition area. Also, the quality of the deposited material tends to be low at such high growth rates, with significant graphitic/non-diamond inclusion.

Other flame-based systems have been developed to improve efficiency and increase the deposition area and diamond quality. These systems incorporate novel nozzle designs for more uniform, larger area flames and may operate at sub-atmospheric pressures. The price paid for improved quality is reduced deposition rates, as in essentially all systems discussed here.

Electron Cyclotron Resonance

Electron cyclotron resonance (ECR) is a process by which microwave plasma generation is enhanced at relatively low gas pressures through the application of a magnetic field in the plasma generation region. Free electrons moving through a magnetic field experience a force ($\vec{F}_B = e \cdot \vec{v} \times \vec{B}$, where e is the electron charge, v is the electron velocity and B is the magnetic field strength) that acts to cause these electrons to follow helical trajectories. The frequency at which an electron executes this cyclic motion, known as the cyclotron frequency, is determined by the magnetic field strength and the charge-to-mass ratio of the electron, as $\omega_c = \frac{e}{m_e} \cdot |\vec{B}|$.

Because the charge-to-mass ratio is inherently fixed, the frequency is controlled solely by the magnetic strength. If the cyclotron frequency is matched to the frequency of an applied oscillating electric field, a resonant condition occurs for the coupling of the electric field energy into the kinetic energy of the electron. A comparison of the type of trajectory expected for an electron traveling in a uniform magnetic field with and without ECR is shown in Figure 2.7.

Provided the electron has a sufficient mean free path between collisions, its kinetic energy, typically expressed as effective temperature (1 eV = 11605 K), will be greatly increased. For microwave fields oscillating at 2.45 GHz, the necessary magnetic field required to achieve resonance is 875 G. Electron energies of greater than 10 eV may be obtained using this process at sufficiently low pressures (i.e. mean free paths allowing several cyclotron oscillations) [Asm90]. These high temperature electrons may then collide with neutral gas species, inducing impact ionization and dissociation and thus forming and sustaining a plasma. Such plasmas are termed "non-thermal" because of the distinct separation in the temperatures of component particles. Ions in an ECR plasma are typically heated to only a fraction of the absolute temperature of the electrons and neutrals are heated to only a few hundred Kelvins. Figure 2.8 provides a schematic representation of the energetic processes that occur in the plasma as they relate to the various plasma components. While true ECR is only considered to occur at pressures below 10 millitorr, significant enhancement of plasma generation may occur at pressures up to 10 Torr [Lax50, Kaw87]. Operation at these higher pressures may be termed "collisionally damped ECR" or "magnetically enhanced microwave" plasmas. Standard microwave plasma generation (i.e., without magnetic field application) at low pressures («1.0 Torr) is hampered by the reduced interaction cross-section of the microwaves with the gas species.

Another notable feature of the ECR plasma system is that it is electrodeless. Standard RF and DC plasma systems use plate electrodes inside the process chamber itself for plasma generation. These are potential sources of contamination due to energetic interaction with the system environment. Elimination of any such electrodes therefore lends itself to reduced contamination of deposited materials. Figure 2.9 shows the schematic of a typical ECR system used for chemical vapor deposition.

ECR CVD of Diamond

Electron cyclotron resonance (ECR) enhanced microwave plasma systems have reportedly deposited diamond at substrate temperatures covering a range from approximately 200 °C or less to 800 °C or more [Mur94, Edd93, Sin92, Wei91, Hir90, Shi92b, Jin94, Oji93, Kom93, Gil97a, Cha92]. These researches cover pressures varying over three orders of magnitude, from 0.01 to 10 Torr, and microwave powers ranging from 300 to 4000 W. Table 2.2 lists the published experimental parameters used by various researchers for ECR-enhanced diamond CVD.

In the work of Hiraki and Wei, et al., which was among the earliest ECR-based diamond CVD research, films were

Table 2.3 Published ECR Diamond Deposition Conditions

Reference	Pressure (Torr)	Temperature (°C)	Microwave Power (W)	Bias	Substrate	Gases	Gas Flow (sccm)
Hir90	0.01 - 50	500 - 900	400 - 1300	DC(+)	Si	$CH_4/CO/CO_2/H_2$	100
Wei90	0.100	500 - 800	800 - 1300	DC(+)	Si, Al	CH_4+CO/H_2	100
Cha92	5	600	900 - 950	DC (+,-)	Si	CH_4/H_2	104
Shi92a	0.01 - 10	400 - 750	550	none	Si	CH_4+O_2/H_2	?
Sin92	0.025 - 0.060	550 - 650	900	DC(+)	Si	CH_3OH/H_2O	50
Edd93	0.01	300 - 500	500 - 700	DC(+)	Si	$CH_4+O_2/CO/H_2$	?
Jin93	0.825	425 - 1050	950	none	Si	CO/H_2	?
Kad93	0.1 - 0.5	800	4000	?	Si	CH_3OH/H_2	?
Kom93	0.6	830	2000	DC(+)	Diamond	CO/H_2	225 - 235
Oji93	0.1	700	1500	DC(+)	Si, Cu, Ni	$CH_4+O_2/H_2/Ar$	?
Man96	1 - 3	300 - 500	500 - 4000	none	Si	CH_4+O_2/H_2	?
Mar96	0.1 - 2	750	1400	DC(+)	β-SiC	CH_4+O_2/H_2	500
Mur96	0.03	600	300 - 400	?	Si	CH_4+O_2/H_2	500
Gil97	0.6 - 1.9	700	1000	none	Si	CH_3OH/H_2	100

deposited at pressures as low as 0.01 Torr and temperatures as low as 500 °C [Hir90, Wei90]. It was stated that a positive electrical biasing of the substrate was necessary for the formation of diamond at pressures below 1 Torr. Use of a negative bias produced a SiC layer on the silicon substrate at low voltage and etched the substrate at higher voltage. Illustrative gas compositions were given as 3 to 5% carbon monoxide diluted in hydrogen [Hir90], although mixtures of methane and carbon dioxide were also referred to [Hir90, Wei90]. Using a gas mixture of 5% CH_4, 10% CO, and 85% H_2, they were able to deposit a diamond film on aluminum at 500 °C [Wei90].

Chang and Mantei [Cha92] reported that the use of both positive and negative bias potentials improved the quality of diamond formation at a pressure of 5 Torr and deposition temperature of approximately 600 °C. They used gas mixtures of approximately 4% methane in hydrogen, which is a relatively high concentration mixture without the addition of oxygen, particularly at the comparatively high pressure used. Reportedly, deposition without the application of a bias under these conditions produced a very poor film exhibiting almost no appreciable diamond peak under Raman analysis and an unfaceted, ball-like morphology. Notable in this work was the use of a tungsten filament for substrate heating. The filament was located in proximity (~6 mm away) to the sample surface and was heated to 2040 °C, which is typical of the filament temperatures used in HF-CVD systems. Therefore, this system may more aptly be considered a hybrid CVD system, operating at lower pressures than typical for hot-filament and microwave plasma systems and utilizing both thermal and electromagnetic activation of the process gases. To avoid drawing significant thermionic electron emission current from the filament, its power supply was electrically isolated from the system.

Low pressure ECR plasma system operation was investigated primarily as a means of nucleation enhancement by Shing, et al. [Shi92a] Operating their system at 10 mTorr with a silicon substrate (600 °C) located outside the active plasma region, ball-shaped diamond microcrystallites were formed on a Si sample surface when using a gas mixture of 15% CH_4 and 10% O_2 in hydrogen. Deposition of high quality diamond was only reported at an operating pressure of 10 Torr. They did not state the use of a bias potential on the substrate during any mode of operation.

Eddy, et al., reported the deposition of good quality diamond films at a pressure of 10 mTorr [Edd93]. Silicon substrates were scratched with diamond particles, cleaned, and exposed to a pure CO plasma at 0.001 Torr with a -100 V bias for 10 minutes as preparation for deposition. Growth gas compositions consisted of either 40% CO or 45% CH_4 + 18% O_2, in hydrogen. Depositions took place outside the plasma region and a positive bias of 40 V was applied to the substrates. Films showed small-grained morphologies with somewhat irregular faceting. Raman analysis showed obvious diamond characteristic peaks with a broad, amorphous carbon background signal. Assuming proper calibration of the Raman system was used, the diamond peaks were significantly shifted to lower wavenumber values of around 1328 cm^{-1}, indicating a tensile residual film stress characteristic.

In the work of Jin and Moustakas [Jin93], diamond films were deposited over a range of temperatures from 425 to 1050 °C at a system pressure of 825 mTorr. A gas mixture of 5% CO and 95% H_2 was used for all depositions, and no bias was applied to the substrates. Faceted diamond films were obtained over the entire temperature range, although no data was provided to establish film quality. They found that the growth rates observed did not follow an Arrhenius behavior with temperature variation and therefore speculated that the growth process for ECR PE-CVD was not determined by surface-reaction mechanisms, but rather by some other process such as hydrogen abstraction.

Low pressure, ECR-enhanced CVD of diamond was also investigated by Kadano, et al. [Kad93] Working with methanol (CH_3OH, 17 - 100%) and hydrogen mixtures, they deposited films at gas pressures of 0.1 to 0.5 Torr. They used substrate temperatures of 800 °C and a 4 kW microwave source. Optical emission spectroscopy (OES) was used to analyze the plasma environment during deposition. CH and OH emission intensities, taken relative to the H_α atomic emission intensity, both increased with increasing CH3OH composition. While OH emission increased with pressure, CH emission decreased. Raman characterization of deposited films showed an improvement in the quality of the diamond, as indicated by reduced diamond peak widths (FWHM), with increasing pressure. They correlated improved quality with increased OH emission and increased growth rates with increased CH emission. Growth rates were observed to decrease with increasing pressure. Finally, they observed that the amount of incorporated hydrogen in their films decreased as OH emission intensity increased.

Komori, et al., investigated homoepitaxial deposition of diamond using an ECR system [Kom93]. They performed their depositions at 0.6 Torr with a gas mixture of 2.5 to 6.8 % CO in hydrogen. Substrates, which were either (100) or (110) oriented, were heated to 830 °C and electrically biased at 70

V. Films deposited on (100) substrates were found to be smoother than films on (110) substrates. Also, they found that the film characteristics of morphology and surface reconstruction, based on RHEED, LEED, and CL measurements, were similar to those of films deposited using methane/hydrogen mixtures.

Another group to investigate the use of bias enhanced nucleation in an ECR system was Ojika, et al. [Oji93]. Using high methane concentration gas mixtures (from 15 - 100%) and negative bias voltages from 0 - 60 V, they observed substantial nucleation enhancement on silicon when using high methane concentrations (>60%) and significant bias voltages (<-30 V) at a substrate temperature of 500 °C. Subsequent diamond depositions were carried out using gas mixtures of 1% CH_4, 1% O_2, 49% H_2, and 49% Ar at 0.1 Torr and substrate temperature of 700 °C. Similar BEN processing and diamond deposition on copper and nickel substrates produced differing results, in which the copper formed a continuous film on its surface while the nickel substrate failed to form any diamond. A silicon substrate undergoing identical treatment formed a discontinuous film and showed evidence of substrate etching. This illustrated the potentially critical aspects of substrate material effects on resultant film formation.

In the work of Marechal and Yamashita [Mar96], an ECR plasma system was used in an effort to produce heteroepitaxial diamond on β-SiC. BEN was applied to substrates of epitaxial SiC on Si wafers using methane/hydrogen gas mixtures at various pressures from 0.1 to 2.0 Torr. Diamond growth proceeded using a positive substrate bias of 30 V and 2% CH_4/1% O_2/97% H_2 gas at 0.3 Torr. Input microwave power was 1400 W. They found that BEN provided significant increase in nucleation density and that, for all but the lowest pressure investigated (0.1 Torr), a significant fraction of nuclei were oriented with the substrate and showed a dependence on the applied bias voltage.

Murai, et al., published their results on the development of an ECR enhanced plasma system using a non-standard magnetic geometry [Mur96]. They used ring-shaped SmCo magnets to form a planar ring-cusp field in a reentrant coaxial microwave cavity. This essentially placed the magnets above the microwave transmission window, providing "...Radially uniform plasmas generated with microwave powers of 300 - 400 W." Using a gas mixture of 4% CH_4 and 2% O_2, they demonstrated diamond deposition at 30 mTorr using a substrate temperature of 600 °C. Although the use of a substrate bias was not stated in their article, the provided system schematic clearly indicated a biasing circuit for the substrate mount.

Finally, Mantei, et al., presented diamond CVD results from yet another variant of the ECR system. In their work, a FE-Nd-B magnet was located centered above the microwave transmission window, just behind the microwave waveguide entrance and close enough to provide the necessary field within the plasma region. Langmuir probe and emission analysis showed the ion currents and atomic hydrogen emissions were higher with the magnetic enhancement than without. They used a 4 kW capacity, pulse-modulated microwave source with a duty cycle of 0.8 msec on and 7.5 msec off. This system provides hydrogen dissociation without excessive electron or ion bombardment effects and reduces incidental substrate heating. Emission study of the plasma showed a linear increase in atomic hydrogen (alpha) emission with increased peak microwave powers up to 3 kW at a pressure of 1.0 Torr. They claimed diamond growth rates of 20 - 50 times higher when using the pulse-modulated microwave than when using a continuous microwave source at the same average power (300 W). Using a gas mixture of 13% CH_4 and 12% O_2 in hydrogen at a total pressure of 3 Torr, they deposited diamond films on silicon at temperatures from 500 to 300 °C with an average microwave power of 300 W (peak power of 3 kW). Growth rates, ranging from 80 to 200 nm/hr, showed an Arrhenius behavior, from which they calculated an activation energy of 14.9

kcal/mol. Non-diamond content, as determined by Raman spectroscopy, increased with decreasing deposition temperature.

In summation of these various reports of ECR-assisted diamond deposition, there are several factors that appear to be common. Most researchers found the positive electrical biasing of substrates beneficial or even necessary to the deposition of good quality diamond films, particularly at pressures below 1 Torr. Bias enhanced nucleation is effective at low pressures and temperatures in an ECR-enhanced system. When operating at low pressures, gas mixtures tend to be very "carbon rich", with high percentages of source monomers compared to more standard, higher pressure systems.

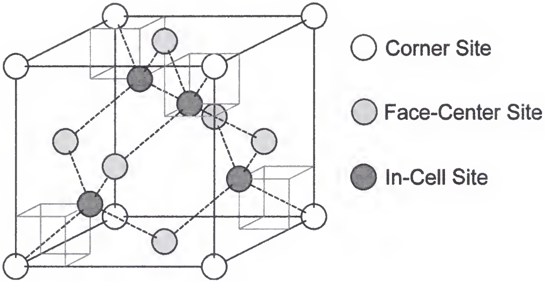

Figure 2.1 Schematic diagram of diamond cubic lattice structure.

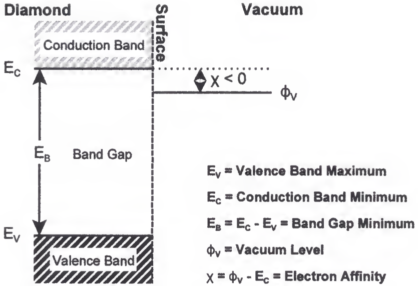
Diamond
Surface
Vacuum
Conduction Band
E_C
χ < 0
φ_V
E_B
Band Gap
E_V
Valence Band
E_V = Valence Band Maximum
E_C = Conduction Band Minimum
E_B = E_C - E_V = Band Gap Minimum
φ_V = Vacuum Level
χ = φ_V - E_C = Electron Affinity

Figure 2.2 Schematic diagram of a negative electron affinity surface.

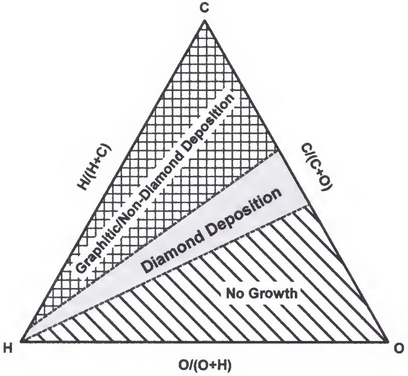

Figure 2.3 Representation of the Bachmann triangle of gas composition for the deposition of diamond in the C/H/O system.

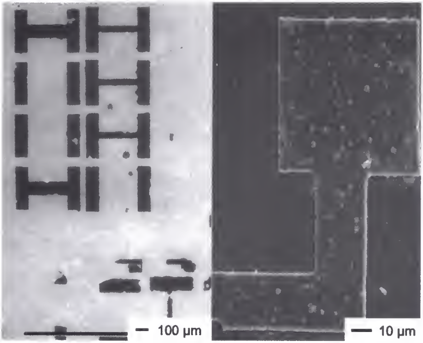

Figure 2.4 SEM images of photolithographically defined diamond film structures.

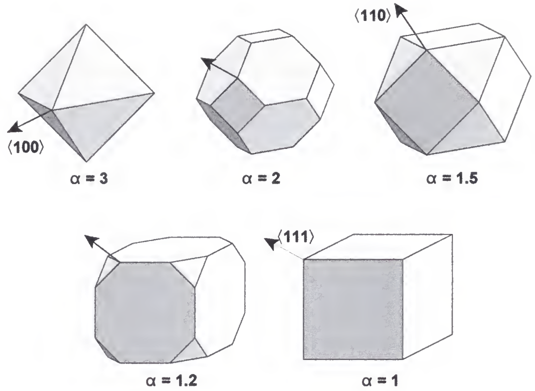

Figure 2.5 Ideal regular crystal structures showing the direction of fastest growth and their corresponding growth parameter.

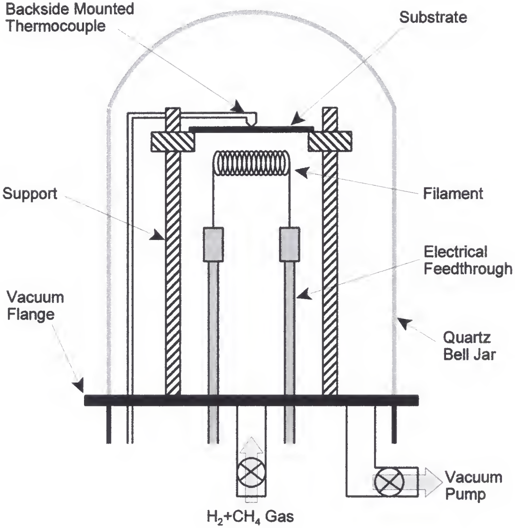

Figure 2.6 Schematic drawing of typical hot-filament diamond CVD system.

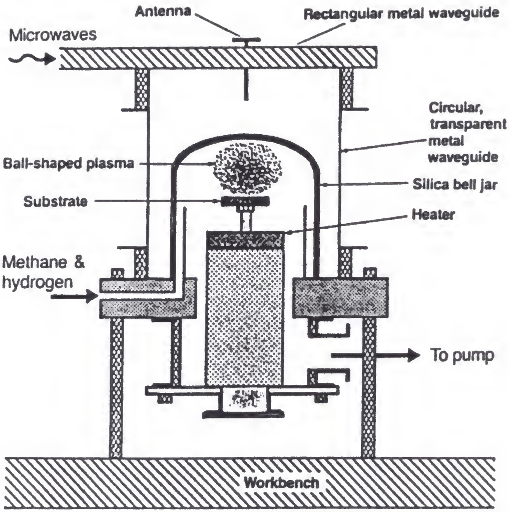

Figure 2.7 Schematic drawing of typical microwave PE-CVD system.[Kob93]

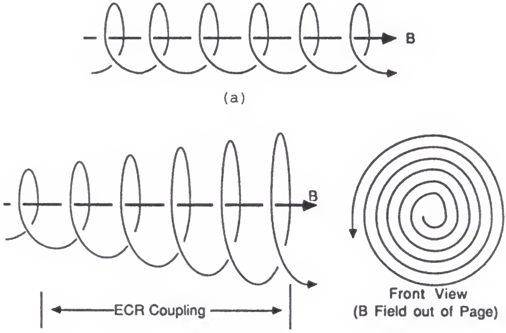

(a)

(b)

Figure 2.8 Examples of electron trajectories in a uniform magnetic field (a) without and (b) with ECR coupling effects.[Asm90]

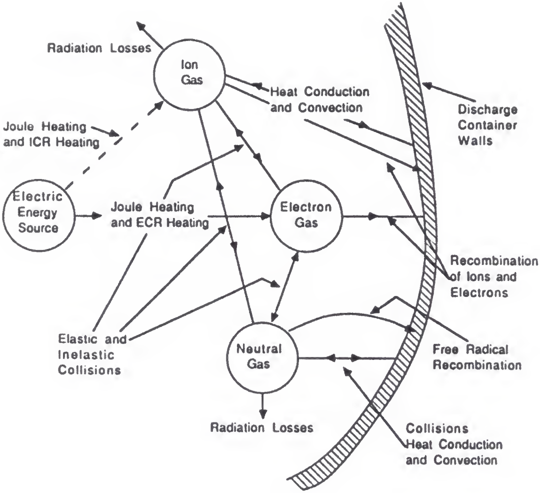
Radiation Losses
Ion Gas
Heat Conduction and Convection
Discharge Container Walls
Joule Heating and ICR Heating
Electric Energy Source
Joule Heating and ECR Heating
Electron Gas
Recombination of Ions and Electrons
Elastic and Inelastic Collisions
Neutral Gas
Free Radical Recombination
Radiation Losses
Collisions Heat Conduction and Convection

Figure 2.9 Schematic representation of energetic processes in an ECR plasma. [Asm90]

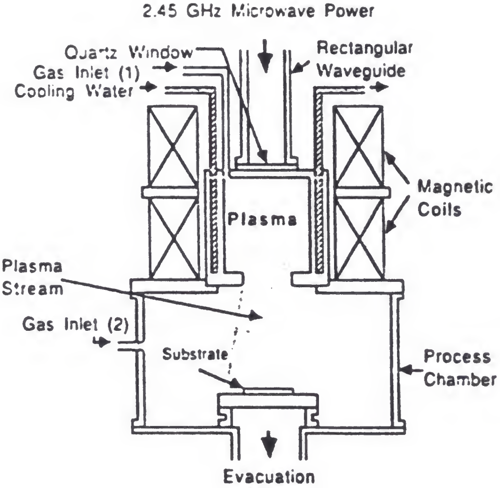

Figure 2.10 Schematic representation of a typical ECR-CVD system using electromagnetic coils. [Asm90]

CHAPTER 3
EXPERIMENTAL SETUP AND PROCEDURES

Diamond Deposition

System Design

Deposition experiments were performed in a custom ECR system (BECR 6), designed and built by PlasmaTherm, Inc. in St. Petersburg, Florida. This system uses a ring of ten permanent rare-earth (Fe-Nd-B) magnets arranged around the plasma generation zone to supply the necessary 875 G field inside the chamber for ECR. An Astex S-1500i microwave power generator with a 1500 W maximum output capacity was used to supply the 2.45 GHz fields for plasma generation. Figure 3.1 shows a diagram of the basic experimental system. Microwaves entered the vacuum chamber through a quartz window (8"D x 0.75"T) positioned at the top of the cylindrical ECR module (6"ID x 6"L). A manually-operated three-stub tuner was incorporated in the waveguide from the microwave generation head to minimize reflected microwave power from the plasma chamber. The vacuum chamber (approx. internal volume: 110 ℓ) was built of aluminum with viton elastomer vacuum seals. Chamber pressure was measured using a MKS capacitance manometer (Baratron Type 124) with a maximum pressure range of 2.000 Torr. Low pressure (≤300 millitorr) operation was sustained using a Leybold-Heraeus Turbovac 450 turbomolecular pump. A Stokes two-stage rotary vane mechanical pump (model# 023-241) was used for system roughing and to back the turbomolecular pump. For higher pressure operation (≥300 millitorr), the chamber was evacuated to the standard base pressure (~ 10^{-5} Torr as determined by an ionization gauge) using the turbomolecular pump and plasma processing was accomplished using only the mechanical pump. Using these two pumping variants, process pressures could be effectively varied from as low as ~5 mTorr to as high as 2.000 Torr.

For deposition at controlled temperatures, samples were placed on a heated mounting stage inside the chamber. This stage could be raised and lowered during system operation to introduce or remove samples from the active plasma region. The stage was heated using silicon carbide resistive heating elements beneath a molybdenum plate. Under typical deposition conditions (1.0 Torr and 1000 W microwave power with samples placed in contact with the plasma) substrates achieved a temperature of approximately 550 °C without applying power to the heater. With the assistance of the heater, substrate temperatures could be raised up to 750 °C.

The primary source monomer species used for growth in this work was methyl alcohol, CH_3OH. Use of this species has certain advantages over the more widely used methane (CH_4) carbon source. Methanol has an inherent 1:1 ratio of carbon to oxygen, which has been widely shown to be a common composition characteristic in the deposition of high quality diamond, especially at relatively low temperatures[]. Also, as a liquid source, it is readily available in high purity form and is easily handled without the need for high pressure tanks and regulators. Liquid methanol was kept in an evacuated stainless steel reservoir for deposition. Regulation of the flow of methanol vapor into the system was accomplished using a needle valve. Flow rate was set before each deposition using a standard calibration procedure, based on measuring the rate of pressure increase in the closed (unpumped), evacuated chamber when allowing methanol vapor to flow. Hydrogen made up the bulk of the deposition environment under standard conditions and was regulated using an electronic mass flow controller (Brooks model 5850E). All other gases used in this system were regulated by electronic mass flow controllers. Comparison of measured pressure increase rates between the calibrated needle valve and the mass flow controllers showed excellent agreement.

Sample Preparation

Over the course of this research, several different procedures were used to prepare samples for deposition. As described previously, nucleation enhancement is critical to the effective deposition of continuous diamond coatings on non-diamond substrates, particularly under relatively low temperature conditions.

Particle abrasion

The earliest experiments conducted in this plasma system used substrates that were manually scratched using diamond particles in slurries and polishing compounds. Later, abrasion of substrates was accomplished by submersing the sample in a suspension (colloid) of diamond particles in an ultrasonic bath. Ultrasonic abrasion provided significantly better uniformity and consistency for sample surfaces than manual scratching.

Electrophoretic seeding

When particle seeding of substrates became desirable, the use of an electrophoretic deposition system was investigated. In this process, the substrate was anodized in a colloidal suspension of diamond particles similar to that used for abrasion processing. The inherent negative zeta potential of the diamond particles provided a motive force to attract them to the positively biased substrate. This process is illustrated in Figure 3.2. While this procedure was capable of effectively seeding common silicon substrates, it could not be used for insulating materials such as sapphire. Also, areal uniformity and consistency proved to be problematic. However, it was shown that this technique was capable of providing seed layers with statistically preferred (111) crystallographic orientation [Lee97].

Electrostatic seeding

Submicron-sized diamond particle seed coatings were deposited on silicon wafers using a novel electrostatic-based process that was developed in the course of this work [Ste94, Car97, Gil97b]. In this process, a monolayer of cationic polymer, specifically poly(ethyleneimine) (PEI), was adsorbed from an aqueous solution onto the native oxide layer of the silicon surface, which has an inherent negative surface charge in water. Thereafter, an aqueous colloidal suspension of diamond particles was introduced to the surface. As a result of the inherent positive charge of the PEI layer and the negative zeta potential of the diamond particles in water, an attractive electrostatic force acted to promote deposition of diamond particles on the polymer-coated surface. This is shown schematically in Figure 3.3. The areal density of particles deposited was controlled by the loading (weight percentage) of powder in the colloid, all other factors (e.g., exposure time) being maintained constant. Early implementation of this process used a simple dip-coating procedure, where substrates were submerged in PEI solution for a short time, rinsed to remove excess solution, then submerged in the diamond colloidal suspension for a designated time. While this procedure allowed fair control of the average surface particle density, there were significant problems in areal uniformity. However, seeding by this method was found to be highly consistent and uniform when used in a spin coating procedure. Samples were mounted in a standard spin coater (Headway Research) of the type used for applying photoresist in the fabrication of microelectronic semiconductor circuits. PEI was then spun onto the sample surface, followed by diamond colloid. This process also had the advantage of reducing waste material in processing, as all suspension (enough to cover the entire substrate) used in dip coating got contaminated and was discarded while only a few drops of PEI and colloidal solution were required to effectively seed a silicon wafer of 2" diameter. As previously mentioned (Chapter 2), this process may be combined with photolithographic processing [Ste94] to provide well defined diamond film structures that may be useful in microelectronic and micromechanical applications (Figure 2.4).

Deposition Procedure

Although particular aspects of individual depositions varied as to parameter settings and time of processing, certain basic procedures were followed for essentially all experiments conducted in the ECR system. Substrates were normally prepared by one of the methods described above. When samples were ready for processing, the chamber was opened and samples were manually placed on the mounting stage inside. The chamber was then closed and the system pumped down to base pressure (approximately 10^{-5} Torr). Following this, methanol flow would be calibrated for the desired rate, as described previously, if it was to be used in the experiment. Samples were then ramped up to approximate deposition temperature using the heated stage. A hydrogen plasma was then lit with the substrates positioned outside the active plasma area. The plasma was tuned (using the sliding short and three-stub tuner) to minimize the amount of reflected microwave power in the waveguide. Samples were then moved into position for processing, typically in contact with the plasma. After a few (2 to 5) minutes exposure to the hydrogen plasma to help remove any residual organic surface contaminants, the gas was changed to the deposition composition. The system often required some re-tuning following the change in gas composition. Because of transient effects, the system had to be monitored continuously for the first 15 - 30 minutes (or more) of the deposition, and periodically (15 - 60 minute intervals) checked for the rest of the deposition duration.

After the designated deposition period, the plasma was change back to pure hydrogen. Samples were left in this plasma for 1 - 2 minutes, then moved out of the plasma region. The plasma was then terminated and the sample temperature ramped down to room temperature. After venting the system to atmospheric pressure using pure nitrogen, the chamber was opened and samples were manually removed. The system was normally left under vacuum between experiments.

Characterization

Microscopy

Surface-specific microscopies, such as scanning electron microscopy (SEM) and atomic force microscopy (AFM), provide very basic information regarding resultant film morphology and roughness. Observation of film morphology provides information about the growth characteristics of the deposited diamond [Sap94]. Excessive twinning and renucleation produce films with an irregular "cauliflower" morphology, lacking clear faceting. Individual crystal shape provides evidence of which crystallographic direction (i.e., growth parameter) has the fastest growth rate for the deposition conditions being used. Figure 3.4 shows examples of films exhibiting regular faceting and irregular morphology.

Scanning electron microscopy

Scanning electron microscopy (SEM) was performed on samples using a JEOL JSM 6400 scanning electron microscope to determine film morphology and crystal size. Typically, samples were examined using a 15 kV accelerating voltage and a 15 mm working distance. Although high purity bulk diamond is highly insulating and therefore subject to charging effects that make imaging very difficult without the use of thin conductive coatings such as gold or graphite, the thin (≤1-2 µm) polycrystalline films of this work typically posed little or no problems.

Atomic force microscopy

Atomic force microscopy (AFM) was also performed on some deposited films using a Digital Instruments Model Nanoscope III. This instrument accommodates samples up to ~0.5" in diameter. AFM has the advantage of being insensitive to the electrical conductivity of the materials examined, making examination of diamond films on any substrate possible without any need for conductive coatings. Also, AFM provides truly quantitative information regarding surface features as it records height data, from which various aspects of the surface roughness may be calculated. Due to the inherent roughness of the polycrystalline diamond films, AFM was performed in contact mode, with the stylus being dragged across the surface of the sample, to eliminate any error due to over-compensation that can occur in tapping mode for such surfaces.

Micro-Raman Spectroscopy

Background

Deposited material was characterized using micro-Raman spectroscopy. Raman spectroscopy is a popular and powerful tool in the analysis of diamond films [Shr90, Bou91, Age91, Ber97]. It provides a relatively simple means of determining the presence of the diamond phase in a carbon film. Analysis is nondestructive and, for standard observation, there is essentially no sample preparation required. Raman shifted radiation is the result of interaction with the structure of the crystalline solid whereby the energy lost by the probe radiation coincides with the generation of a phonon (in the case of the more common Stokes scattering). Inelastic Raman scattering of probe illumination (typically the 514.5 nm line of an argon ion laser) by diamond produces a characteristic peak in the scattered spectrum at a shift of approximately 1332 cm^{-1}. Polycrystalline graphitic (sp^2 bonded) carbon produces broad Raman spectral peaks around 1580 (G-band (graphitic)) and 1360 (D-band (disordered)) cm^{-1} and has a

Raman scattering efficiency approximately 50 times greater than diamond, making it a sensitive probe of film phase purity [Shr90]. However, accurate quantitative analysis of phase composition via Raman is difficult due to variations in optical properties in films based on factors such as average crystal size and surface roughness. The relative sensitivity of Raman scattering to sp^2 bonded carbon is also dependent on the wavelength of the probe illumination. Longer wavelength radiation is more sensitive to graphitic constituents, while shorter wavelength illumination becomes relatively insensitive to graphitic content [Bou91]. Table 3.1 lists some common relevant Raman signatures and their scattering peak shift positions.

Table 3.1 Characteristic Raman Spectral Features

Material	Peak Position (cm^{-1})
a-Diamond (sp^3 bonded a-C)	1140
Diamond (sp^3 bonded C)	1332
Graphite (sp^2 bonded C)	~1360 (D-band), 1580 (G-band)
Polyacetylene (a-C:H)	~1450
Broad a-C band	~1200 - 1600

Along with its value in compositional characterization, Raman may be used for analysis of residual stress in diamond [Age93, Rat95, Ber95]. Strain in the crystalline lattice modifies the elastic constants acting between the carbon atoms, causing a shift in the characteristic diamond scattering peak from its unstressed position. Compressive stress results in shifts to higher peak values, while tensile stress produces lower peak values. The magnitude of the stress can be estimated from the amount of the shift from the unstressed position. If the stress is sufficiently large and non-hydrostatic (e.g., biaxial), a resolvable splitting of the previously degenerate phonon modes will occur, producing multiple characteristic peaks. For an unsplit diamond peak, the proportionality constant for the stress induced offset of the characteristic diamond peak is approximately -1.62 cm^{-1}/GPa [Ral95], although this value may vary depending on the exact characteristics of the film, such as phase purity.

Crystalline defects and intrinsic stress in a polycrystalline film cause both broadening and shifting of the diamond peak relative to that of a single crystal diamond. The two primary sources of broadening of the Raman diamond peak are homogeneous broadening and crystal domain size effects. Homogeneous broadening occurs due to the reduction of phonon lifetimes by defect structures in the crystalline lattice. As domain size decreases, the number of allowed phonon frequencies increases due to quantum uncertainty ($\hbar \propto \Delta\text{Linewidth} \times \Delta\text{Lifetime}$). Homogenous broadening produces a symmetrical line shape of the Lorentzian type. Domain size broadening is expected to be asymmetrical and to be accompanied by a shift to lower wavenumbers [Ber97].

Raman analysis consists of two primary configurations: standard (or "macro-") Raman spectroscopy, where the probing laser is focused using standard optics to spot sizes on the order of a millimeter; and micro-Raman, where an optical microscope is used to produce spot sizes down to the micron scale. Micro-Raman analysis, which uses a back scattering geometry, accommodates very localized analysis for the examination of individual grains or grain boundary regions in polycrystalline samples, and allows depth profiling in thick films. Standard Raman, which is typically done with a low-angle (>45° from surface normal) incident-beam geometry for film samples, provides bulk average scattering properties for the illuminated area (≥ 1 mm^2). Schematic representations of a common Raman setup shown in Figure 3.5. Figure 3.6 shows macro-Raman spectra of a (110) single crystal diamond chip along with one from a high quality, free standing diamond film for comparison. This figure clearly shows the shifting and broadening phenomena previously described.

Sample characterization

Micro-Raman analysis in this work was performed using two different spectrometer systems. For some samples, a Jobin Yvon T64000 triple spectrometer with a 0.64 m focal length and 0.1 cm^{-1} spectral resolution was used for spectral evaluation. An argon ion laser was used to provide the probe illumination using the 514 nm emission line. The resolved spot size of the incident laser beam was approximately 1 - 3 µm in diameter. Other samples were examined using a Jobin Yvon Ramanor U1000 double spectrometer with a 1 m focal length. This system also used the 514 nm argon line with a spot size of approximately 3 microns. Spectral resolution in this system was approximately 1.0 cm^{-1}. Pictures of both types of systems are shown in Figure 3.7.

Raman spectra were analyzed using SPSS Peakfit™, which is commercial software specifically designed for the fitting of peak functions to spectral data. This software allows the simultaneous fitting of many peaks with a variety of possible functions (e.g., Gaussain, Lorentzian, etc.) and offers several different possible spectral baseline approximations. Use of this software provides a systematic method to determine spectral characteristics such as peak centers, widths (full-width-at-half-maximum or FWHM), and peak area (integrated intensity). As mentioned above, the characteristic diamond peak primarily exhibits Lorentzian type spectral line broadening,

$$y = a_0\left(1+\left(\frac{x-a_1}{a_2}\right)^2\right)^{-1}, \qquad (3.1)$$

where a_0, a_1, and a_2 are the peak amplitude, center, and width, respectively. However, due to various instrumental sources, acquisition of the spectrum imposes Gaussian broadening on the data, thus making both the Lorentzian and Gaussian fit inaccurate. The Voigt function incorporates a convolution of these two types of spectral broadening, thus allowing a more accurate fit, and takes the following form:

$$y = \frac{a_0 \int_{-\infty}^{\infty} \frac{\exp\left(-t^2\right)}{a_3^{\,2} + \left(\frac{x - a_1}{a_2} - t\right)^2} dt}{\int_{-\infty}^{\infty} \frac{\exp\left(-t^2\right)}{a_3^{\,2} + t^2} dt}. \tag{3.2}$$

Here, a_0 and a_1 are the peak amplitude and center, while a_2 and a_3 are the gaussian width and shape (proportional to the ratio of the Lorentzian and Gaussian widths), respectively. All Raman spectra in this work were fit using the Voigt function.

Optical Emission Spectroscopy

Optical emission spectroscopy (OES) is a common characterization method used for analyzing plasma discharges. The radiant emissions of a plasma are comprised of the characteristic emissions of its constituent components, consisting of neutral atoms and molecules (including radicals), and ions. Through the use of an optical spectrometer, these emissions may be identified and their behavior studied as a means of process characterization. OES is relatively easy to implement, requiring only the provision of a suitable optical path to the plasma region. However, this characterization is not sensitive to all species present in the plasma because it is based solely on the optical emission of the plasma species. While many excited species return to the ground state by radiative emission, some may make the transition through non-radiative processes. Therefore, OES can only detect species that emit photons within the spectral range of the detector and at sufficient intensities to separate them from the noise level. Quantitative measurement of species based on optical emission is difficult due to the many factors which influence emission intensity, such as particle collision frequency, probability of specific transitions, etc.

OES was performed using an Ocean Optics, Inc., PC1000 PC Plug-in Fiber Optic Spectrometer. This spectrometer was incorporated on a 500 KHz analog-to-digital data acquisition board that plugged directly into an expansion slot in a standard PC-compatible computer. Figure 3.8 shows a picture of this type of board-mounted spectrometer. A diffraction grating with 600 lines/mm, blazed at 500 nm (maximum efficiency), provided a spectral bandwidth (i.e., efficiency >30%) from 350 to 850 nm. Light was collected through a 400 µm diameter optical fiber and the detector (a 1024 pixel element linear CCD silicon array) had a 10 μm entrance slit. The resulting spectral resolution of this system was approximately 1.5 nm. Our spectrometer was installed in a 80486 DX-2 66 MHz computer with 16 MB of memory. Spectra were obtained and saved as two-column (wavelength, intensity) ASCII data files using OOIBase™ (Ocean Optics, Inc., Basic Acquisition Software), designed for use with the Microsoft Windows™ operating system.

Plasma emission from the ECR system was observed through the quartz microwave-transmission window at the top of the vacuum chamber using a fiberoptic cable, as shown in Figure 3.1. Spacial non-uniformities in the plasma and inherent inconsistencies in microwave "tuning" (minimization of power reflected from the plasma region) produced variations in the observed spectral intensities due to the limited optical collection volume of the spectrometer. Also, to get the highest level of sensitivity, the integration time for spectral acquisition was modified for each plasma depending on the system conditions (i.e., pressure, power, and composition) to maximize the amount of signal collected by the CCD detector. Therefore, in order to make the most consistent direct comparisons among different spectra, a normalization procedure was carried out on each collected spectrum to provide a common scale. This procedure is most applicable for spectra (i.e., plasmas) with a high degree of similarity, i.e., from gases of very similar composition (such as ~99% hydrogen) at the same pressure and input microwave power.

For the greatest possible spectral accuracy, the spectrometer was calibrated immediately before taking spectra. Calibration was performed using the four strongest visible atomic emission lines from a pure hydrogen plasma, which were the 410, 434, 486 and 656 nm lines of the Balmer series (typically referred to as delta, gamma, beta, and alpha, respectively) [Lid90]. Spectral calibration in this unit uses a quadratic fitting of wavelength to CCD pixels, as:

$$\lambda = \lambda_0 + C_1 \cdot p + C_2 \cdot p^2. \tag{3.3}$$

Here λ is the measured wavelength, λ_0 is the minimum observable wavelength (i.e., at pixel 0), C_1 and C_2 are the fitting (calibration) coefficients, and p represents the pixel number of the detector.

The PC1000 spectrometer can correct for the electronic "dark" signal contribution to measured spectral intensity, automatically taking into account the integration time used for data acquisition to keep the spectral base-line near zero. To further reduce random noise in acquired spectra, the spectrometer can dynamically average successive spectral samplings. Statistically, the random noise component of the spectrum decreases as $(\sqrt{n})^{-1}$, where n is the number of samples averaged (i.e., averaging over sixteen successive samplings reduces random noise contributions to the data to 25% of the single-sample value). For a steady state emission source such as that produced by an ECR plasma, a large number of samples (up to 30) can be dynamically averaged, significantly improving the signal-to-noise ratio for examination of weak spectral features. Finally, in order to properly remove systemic contributions to the acquired spectrum, a reference dark-spectrum must be taken (by simply blocking off light collection by the fiberoptic) and subtracted from the collected emission spectrum. The effectiveness of this noise reduction and subtraction procedure is illustrated in Figure 3.9, which shows spectra taken from common fluorescent room lights. Here, the wavelength range was taken from 675 to 850 nm to show the minor emissions from argon in the fluorescent lamp. As this figure shows, both dynamic averaging and dark-spectrum subtraction are necessary for optimum spectral examination.

To a first approximation, the optical emission of the diamond-growth-composition plasma can be regarded as a sum of the emission from the hydrogen component and emission from the non-hydrogen components of the plasma, as:

$$I_{gc}(\lambda_i) = I_{H}(\lambda_i) + I_{NH}(\lambda_i). \tag{3.4}$$

Here $I_{gc}(\lambda_i)$ is the acquired spectral intensity at wavelength

λ_i, $I_{H'}(\lambda_i)$ is the intensity contribution due to hydrogen emission, and $I_{NH'}(\lambda_i)$ is the intensity due to non-hydrogen components of the plasma at wavelength λ_i. The prime (′) notation is used here to indicate that the emission characteristics of the separated components do not actually match those of a plasma of that pure component, but are modified by the interaction with the other components (e.g., addition via dissociation or subtraction via recombination). This may be written in functional form as:

$$I_{H'}(\lambda_i) = c_i \cdot I_{H^*}(\lambda_i), \tag{3.5}$$

where c_i is the modification factor at wavelength λ_i and I_{H^*} is the emission intensity of the pure plasma at the same power and pressure conditions. The exact value of c_i will depend on the system parameters of feed-gas composition, pressure and input microwave power, and will tend to deviate further from an initial value of 1.0 as system parameters vary. As a result of the above, the spectral emission intensity may be written as:

$$I_{gc}(\lambda_i) = c_i \cdot I_{H^*}(\lambda_i) + I_{NH'}(\lambda_i). \tag{3.6}$$

If a reference spectrum of pure hydrogen at the same pressure and input microwave power, which represents the definition of I_{H^*}, is then subtracted off, the result is:

$$I_{gc}(\lambda_i) - I_{H^*}(\lambda_i) = (c_i - 1) \cdot I_{H^*}(\lambda_i) + I_{NH'}(\lambda_i) \tag{3.7}$$

The modification factor c_i may be close to 1.0 over most of the spectral range for high dilution compositions, i.e., nearly 100% hydrogen, making the first term on the right hand side very small in comparison to $I_{H*}(\lambda_i)$ (it may be positive or negative depending on the value of c_i). By taking care in spectral acquisition and normalization, the non-hydrogen related spectral features may be brought out of the noise level through this subtraction process. This was essential for observing details of the optical emissions of minority components. Figure 3.10 shows a plot of normalized spectra for pure hydrogen and hydrogen with 1.0% methanol added (an example growth composition). Also plotted is the difference between these two spectra, i.e., $I_{gc} - I_{H*}$. This figure clearly illustrates the usefulness of the normalization and subtraction procedure for the examination of minority constituents of the plasma, most of which would be imperceptible otherwise.

Normalization of pure hydrogen and growth composition plasma spectra was accomplished based on the molecular hydrogen emission lines. These lines were chosen because they cover the largest spectral range within the detection limit of the spectrometer and represent the largest compositional component of the plasma, making their removal most desirable for spectral observation. Also, it was speculated that molecular hydrogen emission would experience the least variance as the result of compositional change, being less reactive than atomic hydrogen. As a result, atomic hydrogen lines were typically over- and under-subtracted from the growth composition spectra due to the previously mentioned variance in intensity between the pure hydrogen plasma and the growth plasma, i.e. the c_i factor, which generally correlated with a change in the atomic hydrogen concentration. Because there are only a few, well defined atomic hydrogen lines within the spectral observation range, this "error" was considered negligible for the spectral analysis performed.

As stated previously, direct correlation of emission intensities with the ground-state concentration of a given species is not generally possible due to phenomena such as chemiluminescence and collisional energy transfer processes. However, under certain conditions it is possible to determine relative concentrations of a species using a reference emission from another component of the plasma [Cob80]. This component, known as an actinometer, must be an inert species such as argon, to avoid changes in its relative concentration through reaction processes. By adding the actinometer in known concentrations to the gas mixture, its emission intensity can be used as a reference for the intensities of emissions from other species that have similar excitation energies. As specified in the work of Youchison, et al., valid actinometry requires that species to be measured must decay from excited states through optical emission, have transition energy within 1 eV of the first excited state of the actinometer, and have similar partial ionization cross section thresholds and dependence on electron impact energy [You93].

In the case of diamond deposition plasma chemistries, actinometry is functionally useful only for determining relative atomic hydrogen concentrations.[Sto94] Based on the above mentioned considerations for effective actinometry, the gamma emission line (434 nm) is expected to provide the best reference for atomic hydrogen concentration because its excitation energy lies within 0.5 eV of argon's first excited state (using the 750.4 nm line). However, the hydrogen gamma emission also has an inherently lower signal-to-noise ratio than the beta and alpha emissions. Therefore, all three emissions were measured to provide a basis of statistical comparison. However, when variations in plasma conditions cause a change in the electron energy distribution function (EEDF), which is related to the effective electron temperature, the relative intensities of the three atomic hydrogen emissions change in a disproportionate manner. Therefore, changes in the EEDF also cause disproportionate measured values of the relative atomic hydrogen concentration based on which emission line is measured. As a result, it is important to monitor changes in the EEDF. This may simply be done by observing the behavior of the beta and gamma emission intensities relative to the alpha emission intensity.

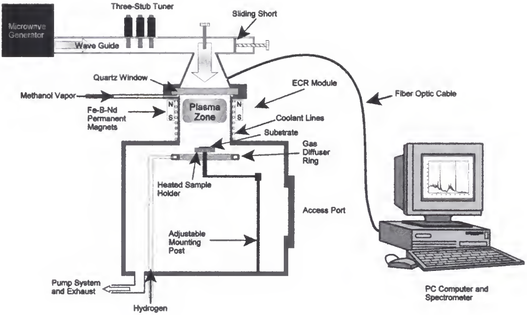

Figure 3.1 Schematic diagram of ECR-enhanced plasma system showing optical spectrometer set-up.

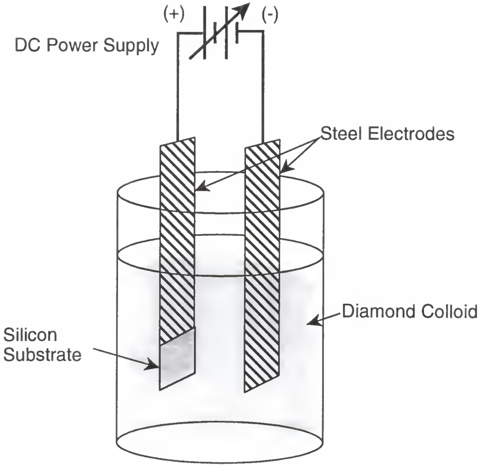

Figure 3.2 Schematic of electrophoretic diamond seeding set-up.

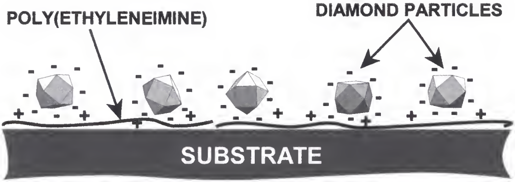

Figure 3.3 Schematic representation of electrostatic-based diamond seeding process.

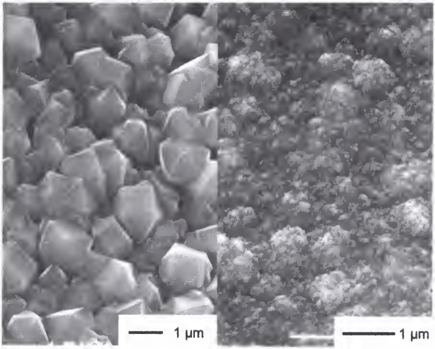

Figure 3.4 SEM micrographs of ECR-CVD deposited films showing well faceted crystallites and excessively twinned and renucleated morphology.

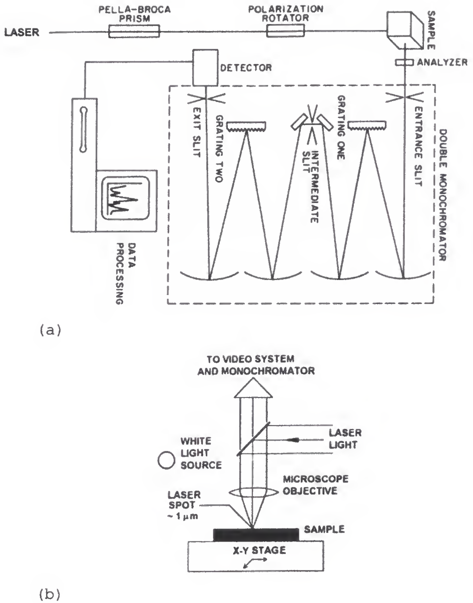

Figure 3.5 (a) Schematic of basic Raman system using a double monochrometer [Whi92] and (b) detail of micro-Raman sample geometry.[Per93]

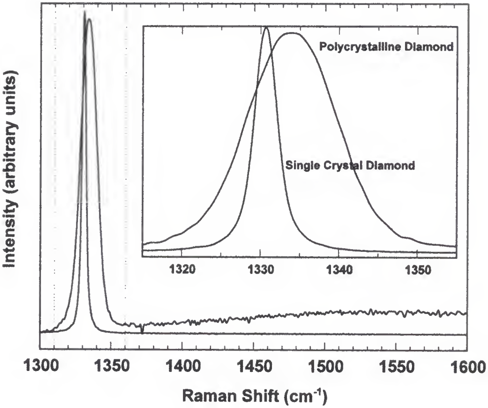

Figure 3.6 Raman spectral plots showing the difference between single crystal (110) diamond and thick, free-standing polycrystalline diamond film.

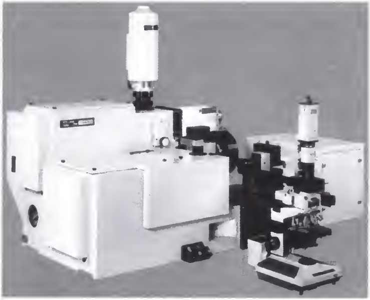

(a)

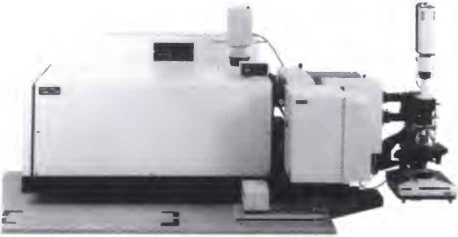

(b)

Figure 3.7 Photographs of Jobin-Yvon (a) T64000 and (b) U1000 Raman spectrometer systems.

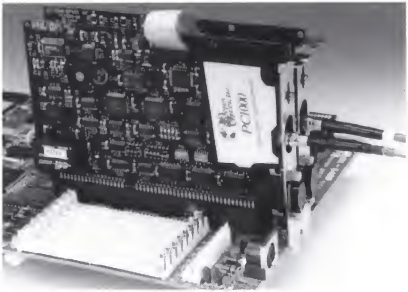

Figure 3.8 Photograph of Ocean Optics card-mounted optical spectrometer.

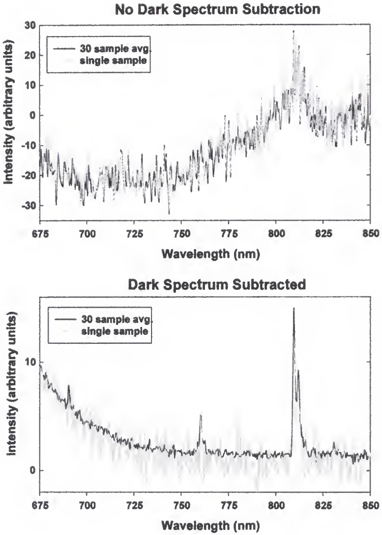
No Dark Spectrum Subtraction

Dark Spectrum Subtracted

Figure 3.9 Optical spectra showing the effectiveness of spectral averaging and dark-spectrum subtraction for argon emission lines taken from a fluorescent room light.

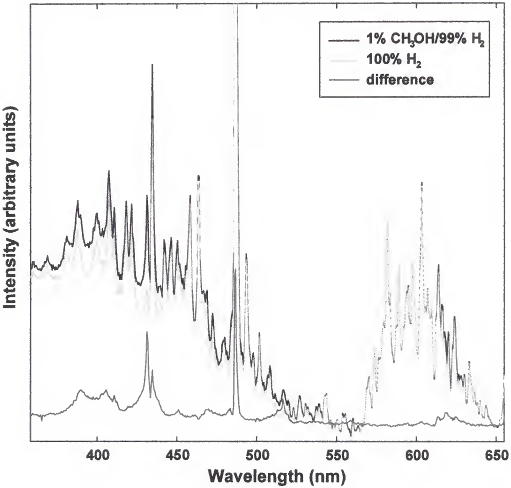

Figure 3.10 Normalized optical emission spectra of growth-composition and reference hydrogen plasmas along with the difference, showing the emergence of non-hydrogen emission details through spectral processing.

CHAPTER 4
RESULTS AND DISCUSSION

Early Experiments

The ECR system was relatively new technology when this research began. Deposition characteristics for diamond in such a system were not well established. Therefore, initial efforts were targeted at determining viable deposition conditions for good quality diamond using the unique capabilities of the system.

Initially, operating conditions of the plasma system were kept near true ECR operation [Sin92], in a pressure regime no greater than 0.100 Torr, which is two orders of magnitude lower than for typical diamond deposition systems. Process gas compositions consisted of methanol and water-vapor mixtures, with methanol as the majority component and some depositions conducted using pure methanol vapor. Substrate temperatures were varied from approximately 400 to 700 °C. A positive electrical bias was sometimes applied to the substrate in an effort to promote remote (i.e., outside the active plasma region) film deposition. Both molybdenum and silicon substrates were used in these early experiments. Substrates were prepared for deposition by manually scratching the surface using diamond-based polishing compounds of different particle size (0.25, 3, and 9 µm) and a cotton swab. Deposition results consisted primarily of nanocrystalline agglomerates consisting mostly of amorphous carbon, as determined by SEM observation and Raman spectroscopy. These deposits were typically ball-shaped, lacking any obvious faceted structure, and often did not develop into continuous films after as much as 12 hours of growth. Often, mechanical properties of these deposits were quite poor, exhibiting a sooty behavior and being easily brushed off with a cotton swab. Deposition rates were quite low, being on the order of 40 to 60 nm per hour. Raman analysis did indicate the presence of diamond in some of the deposits, but experimental consistency proved problematic under these operating conditions.

Some examples of these early depositions are shown in Figures 4.1 - 4.3. All of these depositions were performed with the substrate in contact with the plasma. As these figures show, deposits were ball-like discreet structures that had not formed continuous films after five hours of deposition. Raman spectra showed mostly amorphous and graphitic carbon with some indications of diamond content.

Depositions shown in Figures 4.1 and 4.2 were formed from pure methanol, both with and without substrate biasing. No significant difference was seen between the biased and unbiased deposits under Raman analysis. The deposit of Figure 4.3 showed a significantly improved diamond characteristic peak in its Raman spectrum along with a clear amorphous-diamond (or sp^3-bonded amorphous carbon) peak around 1140 cm^{-1}, as well as a slight alteration of microstructure under SEM observation. The ball-like agglomerates of this deposit appeared more jagged, possibly indicating a greater amount of crystalline structure versus amorphous material. This deposition was formed using a gas mixture of 83% methanol and 17% water vapor, as well as a substrate bias. For operation in this pressure range, it was found that methanol/water ratios less than approximately 3:1 failed to deposit any material on the substrate.

Current Work

Based on the lack of initial success in depositing reasonable quality diamond films under near-true ECR conditions, the plasma-system operating pressure was extended upwards to the 1 Torr range. This change rapidly yielded positive results by producing films showing clear signs of faceting on distinct crystallites. Following this observation, experiments were conducted that were aimed at "optimizing" the production of good quality diamond and providing insight into the parametric-related variation of deposition characteristics. Small studies of the effects of specific system-parameter variation were conducted regarding system pressure, substrate temperature, input microwave power, and gas composition (C/H/O ratios). Raman analysis in these studies was based on spectra obtained using the T64000 system described previously in Chapter 3.

Pressure Variation

Using a gas mixture of 1.2% methanol in hydrogen, depositions were performed at total gas pressures of 0.6, 1.0, 1.5, and 1.9 Torr. Diamond-seeded silicon substrates were kept at 700 °C and the plasma was sustained using 1000 W input microwave power for 5 hours. AFM analysis showed all films had a faceted structure, as seen in Figure 4.4. Average measured growth parameters (as defined in Chapter 2) are shown in Figure 4.5. However, Raman spectroscopy showed almost no diamond peak for the sample deposited at 0.6 Torr, while all others demonstrated obvious diamond peaks around 1333 cm^{-1}, as seen in Figure 4.6. Table 4.1 lists Raman analytical results, as well as the measured growth parameters for these films. Values of diamond peak-width and percent integrated intensity for the 0.6 Torr deposit are listed in parentheses because of the very low diamond signal measured for this sample, which made the error for these values quite large. Raman analytical values are also plotted in Figure 4.7.

Table 4.1 Film characteristics for depositions at different gas pressures using 1.2% CH_3OH in hydrogen at 1000 W microwave power and 700 °C substrate temperature

Pressure (Torr)	Raman Shift (cm^{-1})	Raman FWHM (cm^{-1})	I_D (area)	I_D/I_{ND}	Growth Parameter
0.60	1331.4	(4.8)	(0.29%)	(.16)	1.93
1.00	1333.0	7.8	4.60%	1.38	1.83
1.50	1333.4	10.8	5.22%	1.32	1.61
1.90	1332.9	8.9	5.42%	1.07	1.61

Close examination of the morphology of the 0.6 Torr deposit showed a large fraction of irregular crystallites with noticeable defect structures, particularly on the (100)-type facets. Deposits at higher pressures showed more regular crystallites with less defective faceting. Defects appeared more prevalent on (111) facets than on (100) at higher pressures, which were likely the result of twinning. Examination of average crystal sizes showed the 1.0 Torr film to have the smallest average grains while the 1.9 Torr film appeared to have the largest average grain size and the 1.5 Torr film was intermediate. The grains of the 0.6 Torr deposit appeared larger on average than those of the 1.0 Torr deposit, but, as mentioned, were noticeably more defective.

Raman analysis showed a significant correlation between the diamond peak shift and FWHM, both of which increased to maximum values at 1.5 Torr. This general type of correlation between shift and width values has also been observed by others [Age91]. Integrated intensities for diamond peaks, expressed as a percentage of the total integrated area under the curve, showed consistent increase from 0.6 (which showed almost no diamond content) to 1.9 Torr. However, when examining the peak intensity ratio between diamond and non-diamond, using whichever non-diamond feature happened to be most intense, there was a decrease in value from 1.0 to 1.9 Torr. Consistency and accuracy in this type of semi-quantitative analysis is very difficult due to variations in the morphological characteristics of the films, sensitivity to the total spectral range observed (particularly due to the concomitant variation in the effective baseline) and the high degree of localization of the laser probe. Also noteworthy in the analysis of the Raman spectra of these films was the fact that for all cases, the most intense non-diamond spectral feature was located in the 1400 - 1500 cm^{-1} range, which is indicative of partially crystallized polyacetylene [Mur91].

Optical emission spectroscopy (OES) was performed on plasmas matching the above conditions in an attempt to examine resultant plasma chemistry variations. Figure 4.8 shows plots of the relative atomic hydrogen concentration, as determined by actinometry using argon (at 1.5% of the total gas composition) as a reference, based on the three most intense atomic hydrogen emission lines (alpha (655 nm), beta (486 nm), and gamma (434 nm)) as a function of pressure, and also plots of the beta and gamma intensities normalized by the alpha intensity as a function of pressure. As shown in the plot of the H_β/H_α and H_γ/H_α emission ratios, the relative changes in intensity of the atomic emission lines with pressure were not totally consistent, indicating some variation in the electron energy distribution function (EEDF) with changing pressure. Pressure dependent variation in the relative atomic hydrogen concentration showed some interesting trends. Figure 4.8(a) shows the atomic hydrogen concentration of the methanol containing plasma relative to the concentration for a pure hydrogen plasma of the same pressure. At pressures from 0.6 to 1.5 Torr, the relative atomic hydrogen concentration decreased with the addition of 1.2% methanol, while at 1.9 Torr there was an apparent increase with methanol addition. Figure 4.8(b) shows the measured relative atomic hydrogen concentrations for 1.2% methanol plasmas normalized by the measured value at 0.6 Torr. This plot indicates that relative hydrogen concentration was highest at 0.6 Torr, lowest at 1.0 Torr, and increased with pressure from 1.0 to 1.9 Torr.

Figure 4.9 shows plots of the emission intensities of various non-hydrogen plasma constituents, relative to molecular and atomic hydrogen emission intensities, as well as oxygen, as a function of system pressure for the source mixture of 1.2% CH_3OH in hydrogen at 1000 W microwave power. Normalizing the intensities by atomic emission instead of molecular emission showed a significantly different behavior. In this case, the relative CH intensity increased with pressure from 0.6 to 1.5 Torr and then decreased. O_2 and C_3 emissions both showed substantial relative increases over this pressure range. Relative C_2 emission intensity showed a minimum at 1.0 Torr. It must be emphasized that the emission intensity of a given species is not necessarily directly proportional to the relative ground-state concentration of that species, due to effects such as chemiluminescence and collisional energy transfer processes.

In looking for correlation between optical emission measurements and Raman measurements, it appeared that comparison to atomic hydrogen emissions was more informative than comparison to molecular emission intensities. Raman analysis indicated a trend for diamond content (based on percentage integrated intensity of the diamond peak) to increase in deposited films with increasing pressure. Relative CH emission intensity, which has been correlated with diamond formation by others [Gom93], decreased relative to molecular hydrogen emission while increasing relative to atomic hydrogen emission. C_2 is not generally considered favorable to diamond formation, but has more generally been regarded as a precursor for graphitic/non-diamond deposition [Wan92, Bal93]. Relative to molecular hydrogen, C_2 showed consistent decreases in emission intensity, while C_2 emission increased relative to H_α emission going from 1.0 Torr to 1.5 Torr. The highest relative C_2 intensity was seen at 0.6 Torr in both cases. Another important consideration in this system is the role of oxygen in the deposition process. O_2 emission intensity consistently increased relative to atomic hydrogen emission. Both CH and C_2 emissions decreased relative to O_2 emission with increasing pressure. C_2 showed the largest decrease relative to O_2 going from 0.6 to 1.0 Torr, which correlated with the largest change in Raman characteristics.

Temperature Variation

Films were deposited at substrate temperatures of 550, 600, 700, and 750 °C on similarly diamond-seeded silicon substrates. Gas mixtures of 1.2% methanol in hydrogen were again used at a total system pressure of 1.0 Torr and input microwave power of 1000 W for 5 hours. All samples showed faceted film structures under SEM observation, as shown in Figure 4.11. Average measured growth parameters were plotted as a function of deposition temperature in Figure 4.12. Raman spectra taken from these films are shown in Figure 4.13, while analytical results are tabulated in Table 4.2 and shown graphically in Figure 4.14.

Table 4.2 Film characteristics for depositions at different substrate temperatures using 1.2% CH_3OH in hydrogen at a total pressure of 1.0 Torr and 1000 W microwave power.

Temperature (°C)	Raman Shift (cm^{-1})	Raman FWHM (cm^{-1})	I_D (area)	I_D/I_{ND}	Growth Parameter
550	1333.1	6.7	4.56%	1.57	1.67
600	1333.0	7.8	5.64%	2.53	2.00
700	1333.0	7.8	4.60%	1.38	1.83
750	1332.5	7.4	5.96%	3.07	2.21

As temperature increased, the growth parameter showed a tendency to increase as well, although this trend was not consistent. Deposition at 600 °C showed a larger growth parameter than deposition at 550 and 700 °C, while deposition at 750 °C showed the highest growth parameter in this series. Values of the Raman diamond peak shift and FWHM showed no consistent trends based on deposition temperature over this range. However, a possible correlation was seen between the diamond integrated intensity percentage and the diamond peak shift value. Lower values of integrated intensity occurred at conditions corresponding to higher peak shift values, and vice versa, which could imply a relationship between impurity incorporation and resultant film stress. Values of the percentage integrated diamond peak area and the diamond/non-diamond peak intensity ratio showed a high degree of correlation in their behavior. Maximum values for each occurred at 750 °C, while the 550 °C values were relatively low.

Power Variation

Two series of experiments were carried out that examined the effects of varying microwave power on resultant film characteristics. In these experiments, input powers of 1000, 1200, and 1400 W were used with a process gas composition of 1.0% methanol in hydrogen at total pressures of either 1.0 or 1.5 Torr. Diamond-seeded silicon substrates were maintained at 700 °C during all depositions. Depositions at 1000 W occurred for 8 hours, at 1400 W for 5 hours, and at 1200 W for 8 (1.0 Torr) or 6 (1.5 Torr) hours. SEM micrographs of these films are shown in Figures 4.14 and 4.15, and average measured growth parameters are plotted in Figure 4.16. Tables 4.3 and 4.4 present Raman characteristics along with average measured growth parameters. Raman spectra are shown in Figure 4.17 and plotted Raman analytical characteristics are shown in Figure 4.18.

All films deposited under these conditions showed well faceted crystalline grains. Average measured growth parameters for these films were consistently larger at 1.0 Torr than at 1.5 Torr, which is generally consistent with the

Table 4.3 Characteristics of films deposited at different microwave powers using 1.0% CH_3OH in hydrogen at 1.0 Torr and substrate temperature of 700 °C.

Microwave Power (W)	Raman Shift (cm^{-1})	Raman FWHM (cm^{-1})	I_D(area)	I_D/I_{ND}	Growth Parameter
1000	1333.0	9.3	4.32%	0.86	1.60
1200	1332.8	9.6	1.99%	0.55	1.58
1400	1332.8	13.1	4.12%	0.69	1.66

Table 4.4 Characteristics of films deposited at different microwave powers using 1.0% CH_3OH in hydrogen at 1.5 Torr and substrate temperature of 700 °C.

Microwave Power (W)	Raman Shift (cm^{-1})	Raman FWHM (cm^{-1})	I_D(area)	I_D/I_{ND}	Growth Parameter
1000	1332.9	9.5	16.23%	6.21	1.53
1200	1333.6	12.2	9.65%	2.51	1.55
1400	1332.6	9.6	6.89%	2.01	1.54

pressure-dependent behavior seen previously for depositions from 1.2% methanol at the same pressures (Figure 4.5). Measured growth parameters showed little variation with power over the investigated range and showed no consistent trends. In fact, most measured values for each pressure fell within the standard deviation of the measurement of each other.

Analysis of the Raman spectra (Figure 4.18) over the range 1100 to 1600 cm^{-1} showed a trend for the integrated intensity of the diamond peak to decrease, in terms of the percentage of total integrated intensity under the curve, with increasing power at 1.50 Torr, while the films deposited at 1.00 Torr showed no consistent change over the power range investigated (the low value for the 1200 W deposition is considered a localized variation based on the small probe size). Very similar behavior was observed for the diamond/non-diamond peak intensity ratios. Films deposited at 1.5 Torr showed significantly larger diamond peaks (as indicated by both percent integrated area and relative peak intensity) than those deposited at 1.00 Torr, indicating consistently greater phase purity. The measured diamond peak shift showed no strong trends with increasing microwave power. Peak widths (FWHM) also lacked significant, consistent dependency on microwave power.

Gas chemistry and plasma behavior as a function of microwave power was investigated using OES, as shown in Figures 4.19 to 4.21. H_β/H_α and H_γ/H_α ratios decreased with increasing power for pure hydrogen plasmas at both pressures, indicating a consistent type of change of the electron energy distribution function. However, as a result of this variance, actinometry measurements of relative atomic hydrogen concentrations varied significantly based on which hydrogen emission line was used. For both pressures and all emission lines, actinometry indicated a decrease in atomic hydrogen concentration when increasing power from 1000 to 1200 W, followed by an increase with power at 1400 W. Similar behavior was observed for a 1.0% methanol plasma at 1.5 Torr, as seen in Figure 4.20. At 1.0 Torr, CH and C_2 emissions increased relative to H_α emission with increasing power, while at 1.5 Torr CH decreased, as shown in Figure 4.21. Relative C_3 emission decreased with power at both pressures, as did O_2 emission.

Gas Composition Variation

To examine the level of deposition dependence on gas composition, films were deposited using different source gas compositions with varying C/H/O ratios. In order to change the ratio of carbon-to-oxygen, methane was used as a source gas so oxygen could be varied independently.

Depositions were performed at pressures of 1.0 and 1.5 Torr using different mixtures of methane, oxygen, and, for one case, methanol in hydrogen. Figures 4.22 and 4.23 show SEM micrographs of these films. Films showed clearly faceted crystal grains for most gas compositions and conditions tested. However, Raman spectra, shown in Figures 4.24 and 4.25, showed substantial variation in film characteristics under these conditions. These results clearly indicate the importance of plasma chemistry in determining deposition characteristics.

Actinometry was performed on hydrogen plasmas containing methane at total pressures of 1.0 and 1.5 Torr to examine the change in atomic hydrogen concentration versus a pure hydrogen plasma. Relative atomic hydrogen concentration dropped by approximately 30% with the addition of 1.0% methane at both pressures.

OES was used to examine the effects of oxygen addition to a methane/hydrogen plasma at a pressure of 1.0 Torr and input microwave power of 1000 W. The plasma system could not accommodate the use of argon as an actinometer for the examined mixtures due to an insufficient number of mass flow controllers. However, the large fraction of molecular hydrogen was speculated to provide a relatively constant intensity reference for qualitative analysis of the atomic hydrogen behavior, so long as variations in the EEDF were small. Figure 4.26 shows plots of the H_β/H_α and H_γ/H_α emission ratios for different plasma mixtures using 1.0% methane, hydrogen, and oxygen. The negative value on the x-axis refers to a reference plasma of pure hydrogen at the same pressure and microwave power. Also plotted in Figure 4.26 are the relative ratios of atomic hydrogen emissions to molecular hydrogen emission, normalized to the corresponding value for pure hydrogen, in similar fashion to argon-based actinometry plots of relative atomic hydrogen concentrations (such as seen in Figure 4.20). This plot shows atomic hydrogen emission dropped approximately 50% (relative to H_2) with the addition of 1.0% methane to pure hydrogen, then rose to nearly its initial intensity level with the addition of 0.25% oxygen.

Relative atomic hydrogen emissions peaked around 0.5% added oxygen. Figure 4.27 shows the variation in emission intensity of CH, C_2, C_3, and O_2 relative to the H_α line and a characteristic H_2 emission for the same compositions. All carbon-containing emission sources decreased relative to atomic hydrogen with increasing oxygen content, while they rose to peak values relative to H_2 emission with 0.5 to 0.75% added oxygen. Also shown in Figure 4.27 is a plot of the intensity behavior of carbon-containing emission sources relative to oxygen emission. This plot shows decreases in all the relative intensities as oxygen content increased.

Actinometry was next performed on methanol/hydrogen plasmas to examine their behavior with oxygen addition. Figure 4.28 shows a plot of atomic hydrogen emission ratios (H_β/H_α and H_γ/H_α). Once again, the negative value on the x-axis refers to a reference plasma of pure hydrogen. Ratios showed relatively little change with the addition of oxygen up to 1.5% of the total gas composition, with the largest relative change coming with the initial addition of 1.0% CH_3OH to hydrogen. However, as shown in Figure 4.29, the relative concentration of atomic hydrogen (normalized to the value for a pure hydrogen plasma) increased continuously with increased oxygen addition. Initial addition of 1.0% methanol caused a decrease in atomic hydrogen concentration of approximately

10%. Also shown in Figure 4.30 is a plot of the atomic hydrogen emissions relative to the molecular hydrogen intensity, normalized in the same fashion as just described for the actinometry values. Comparison of the two plots shows a high degree of similarity, providing evidence that comparison of atomic hydrogen emissions to molecular emissions may be used as a rough indicator of concentration behavior under some circumstances, as was done previously for methane (Figure 4.26). Non-hydrogen constituents showed very similar emission trends with added oxygen relative to both argon and atomic hydrogen emission, as shown in Figure 4.30. Carbon-containing emission sources decreased in intensity with increasing oxygen content while oxygen emission increased.

In order to evaluate the significance of the source monomer on the effects of oxygen addition, actinometry was also performed on plasmas of various mixtures of hydrogen and oxygen, without any carbon source, to establish the degree of dependence of atomic hydrogen concentration on O_2/H_2 interactions. Plots of the results are shown in Figure 4.31. Initial addition of 0.25% oxygen caused a substantial apparent increase in the relative atomic hydrogen concentration, on the order of 40 - 50 %, as well as a relatively large change in the EEDF (based on the Balmer line ratio variation). Further oxygen addition resulted in a decreased atomic hydrogen concentration (although still higher than that of pure hydrogen) for compositions up to 1.5%, after which atomic hydrogen concentration again increased.

Finally, OES was performed on plasmas generated in 1.0% CO in hydrogen with added O_2. Figure 4.32 shows values of Balmer line ratios, again indicating changes in the EEDF. Very little change was seen in the ratio values with oxygen addition. Once again, the negative value plotted on the x-axis refers to values measured from pure hydrogen. Also shown are atomic hydrogen emission intensities relative to molecular hydrogen emission, normalized to the same value of a pure hydrogen plasma, as was done for methane. This plot shows that initial addition of 1.0% CO caused a relative increase in atomic hydrogen emissions, but addition of 0.25% oxygen caused a drop in emissions to below the values for pure hydrogen. Further O_2 addition tended to result in slowly increasing emission intensity. Overall variation in the relative atomic hydrogen emissions was smaller than was seen for methane and methanol. Figure 4.33 shows the emission behavior of non-hydrogen constituents in the 1.0% CO plasma. Similar to previously shown results for oxygen addition (Figures 4.27 and 4.30), CH, C_2, and C_3 emissions all decreased relative to atomic and molecular hydrogen and oxygen. Oxygen emission increased continuously with oxygen addition.

The OES analysis of oxygen addition to the different plasmas indicated that plasma chemistry was highly similar for plasmas of similar elemental (C/H/O) composition, regardless of the specific source monomer. Emissions from various non-hydrogen plasma constituents tended to show similar relative emission intensities at the same C/H/O ratios and very similar trends with compositional variation (i.e., oxygen addition). Monomer-based variations in emission behavior were most pronounced for hydrogen related phenomena, showing differences in their relative atomic hydrogen emission trends with oxygen addition.

Variable Seed Densities

In these series of experiments, silicon samples were seeded using the novel electrostatic method described in Chapter 3. Several different weight-loaded colloids (0.001, 0.01, 0.1, 1.0 and 10% diamond, by weight, in water) of ~0.25 µm average particle size were used to establish a batch series of different areal densities of seed particles on silicon. Also, a series of substrates were prepared from as-received silicon by ultrasonic abrasion with diamond particles. These substrates provided a standard for comparison of deposition on seeded substrates. Taking advantage of the relatively large areal deposition capabilities of the ECR system, made possible by the relative low pressure operation regime, these samples

(~1.0 cm^2 each) were processed simultaneously, thus ensuring the highest possible uniformity of deposition conditions within the sample set to elaborate variations in film characteristics due to "nucleation" density. Raman characterization of these batched samples was performed using the Jobin Yvon Ramanor U1000 spectrometer system described in Chapter 3.

Three different series of depositions were performed using these seed-batches. One series used 1.0% methanol in hydrogen at 1.00 Torr and 1000 W microwave power with substrates at temperatures of 550, 600, and 700 °C. The next series was identical in all aspects to the first except for the addition of 0.25% oxygen in the feed gas composition. Finally, three sample sets were deposited at 1.00 Torr and 550 °C with 1000 W microwave power from gas mixtures of either methanol, methane, or carbon monoxide with added oxygen in hydrogen. This last series maintained the same ratios of C/H/O for each deposition, with the intent of evaluating the sensitivity of the deposition to the specific source monomer.

As stated previously, substrates were seeded using colloids of different weight-loadings of 0.25 μm nominal diameter diamond particles to provide different areal seeding densities. SEM micrographs of typical resultant seed layers are shown in Figure 4.34. The areal densities and average separation distances were determined based on these micrographs and are tabulated in Table 4.5. Resultant seeding densities were clearly not linearly dependent on the weight loading of the diamond colloid. As could be seen by SEM, seeding from the 10% colloid effectively formed total coverage of the substrate surface. In fact, a certain amount of particle overlap could be seen in this case. Lower seeding densities showed very good particle separation, with only a small percentage of isolated overlapping. Another observation made from SEM analysis was that there appeared to be a significant increase in the areal density of large particles from the high end of the size distribution in substrates seeded from 1.0% and 10% colloids.

Table 4.5 Average seeding characteristics for different weight-loaded colloids

Weight Loading (%)	Areal Density ($\times 10^9$ cm^{-2})	Average Separation Distance (μm)
0.001	0.0122	2.86
0.01	0.225	0.67
0.1	1.51	0.26
1.0	2.34	0.21
10.0	3.11	0.18

Depositions were made at a series of temperatures using 1.0% methanol in hydrogen at a total pressure of 1.0 Torr and 1000 W microwave power. Representative SEM micrographs of these depositions are shown in Figure 4.35. Not all depositions included a 0.001% seeded substrate, as this was implemented after this series of experiments was begun in order to ensure that isolated crystal morphology could be examined at each condition. Figure 4.36 shows SEM micrographs of material deposited from 1.0% methanol and 0.25% oxygen in hydrogen at identical conditions to those previously stated. Average measured growth parameters for both continuous films and isolated crystals are plotted in Figure 4.37. Isolated crystals generally showed larger measured growth parameters than continuous films, and corresponding deposition without added oxygen typically produced larger growth parameters than with added oxygen. Isolated crystals showed a consistent decreasing trend in growth parameter with increasing temperature, while continuous films showed maximum values at 600 °C deposition. This temperature dependent behavior of the growth parameter for continuous films was similar to that seen previously for deposition from 1.2% methanol at the same temperatures (Figure 4.11), where the measured growth parameter at 600 °C was higher than that at 550 or 700 °C. Low temperature deposits (550 °C) showed the largest variation in growth parameter between gas chemistries of all temperatures investigated.

These plasma conditions were previously investigated by OES, the results of which were shown in Figures 4.28 - 4.30.

Actinometry (Figure 4.29) indicated that atomic hydrogen content was approximately 10% higher in the plasma with 0.25% added oxygen in the feed gas than without. Also, the relative intensities of CH, C_2, and C_3 (compared to hydrogen and oxygen) all decreased with the addition of oxygen.

AFM measurements were performed on all films produced in these experiments. RMS surface roughnesses were determined from these measurements and are shown in Figure 4.38. Surface roughness decreased from the 0.01% to the 0.1% seeded samples at all deposition conditions. For progressively higher seed density samples, measured roughnesses showed relatively little consistent variation, with measured increases and decreases. For both growth compositions, deposition at 550 °C showed an increased roughness at 10% seeding over 1.0% seeding, while at 600 °C the opposite trend was seen. Samples deposited at 700 °C showed the smallest overall range in measured surface roughness. The most probable reason for the observed roughness variations at higher seeding densities is the previously observed increase in the density of larger seed particles. These particles grow faster than the smaller particles resulting in larger average grain sizes than would otherwise be expected based solely on areal particle density.

Looking at the collective (averaged over all seeding densities) Raman characteristics for films deposited at different temperatures with and without added oxygen (shown in Figure 4.36), films deposited with added oxygen had lower diamond peak shifts at 550 and 600 °C than those deposited without added oxygen. The largest average peak shifts for both mixtures were seen in films deposited at 550 °C. Peak width values were very close for both gas chemistries at 600 and 700 °C and were largest in films deposited at 700 °C. Examining the relative diamond peak intensity characteristics, shown in Figure 4.37, the percentage integrated area increased with increasing temperature for both gas chemistries, though more prominently for those without added oxygen. This trend did not appear in the peak intensity ratio between diamond and non-diamond Raman features. The largest chemistry-based value differences in Raman phase-purity analysis were seen for the 550 °C depositions.

Trends for individual seeding densities were difficult to track consistently, as may be seen in Figures 4.41 - 4.44. Depositions without added oxygen tended to show decreasing trends in both diamond shift and FWHM with increasing particle density (Figure 4.41). Diamond peak shift behavior relative to seeding density was similar for depositions at 600 and 700 °C, with minimum values at the highest seeding density. Examination of the FWHM versus diamond peak shift showed values tended to cluster based on the deposition temperature.

Seeding-based effects in films deposited with added oxygen appeared less obvious, although overall correlation between shift and FWHM (Figure 4.43) was similar to that of depositions without oxygen (i.e., temperature based clustering of values was obvious). Depositions at 550 and 600 °C showed similar FWHM behavior, with maximum values for seed densities of 1.5×10^{9} cm^{-2}. Diamond peak shift values showed little correlation among different seeding densities at different temperatures.

Depositions at 700 °C, both without (Figure 4.42) and with (Figure 4.44) added oxygen, showed similar trends for density based variation in percentage integrated area of the diamond peak. Depositions at 600 °C showed maximum intensity values for the 1.0% colloid seeded samples. Comparison of fractional integrated areas of the diamond peak to the diamond/non-diamond peak intensity ratios showed a relatively high level of correlation for both deposition chemistries.

To further investigate the deposition behavior of the ECR-enhanced diamond CVD, depositions were performed using different source monomers in gas mixtures maintaining the same C/H/O compositional ratios. The gas flow rates used for deposition were as follows (in units of standard cubic centimeters per minute (sccm)): 2.0 CH_3OH/ 0.5 O_2/ 200 H_2, 2.0 CH_4/ 1.5 O_2/ 200 H_2, and 2.0 CO/ 0.5 O_2/ 204 H_2. SEM micrographs of the resultant deposited material are shown in Figure 4.45. Average measured growth parameter values are plotted in Figure 4.46 and listed (continuous film values) in Table 4.6.

Table 4.6 Averaged values of characteristics for films deposited using different monomers on variably seeded substrates at 1.0 Torr and 550 °C.

Monomer	Raman Shift (cm^{-1})	Raman FWHM (cm^{-1})	I_D (area)	I_D/I_{ND}	Growth Parameter
CH_3OH	1335.3	8.1	9.67%	3.51	1.68
CH_4	1334.8	8.5	8.51%	3.42	1.78
CO	1334.9	7.1	8.98%	3.51	1.71

Observation of the SEM micrographs in Figure 4.45 showed films deposited from different gas mixtures on the same areal density seeding had very similar morphology. The methanol mixture showed slightly more crystal grains per area than the other mixtures on 0.001% seeded substrates where grains were effectively isolated from one another. This may have been attributable to localized variation in the seeding density. However, a similar trend was noticed for the 0.01% seeded substrates, which did not achieve full coalescence within the deposition time used, suggesting a possible minor difference in the deposition process environment. As seen in Figure 4.46, there was some variation in the average measured growth parameters based on the source monomer, with the methane chemistry showing the highest value. As seen previously, the average growth parameters of isolated crystal grains tended to be larger than those in continuous (coalesced) films. Both isolated grains and continuous films showed the same relative trends based on the source monomer.

Raman analysis was also conducted on these samples. The diamond peak shift values, shown in Figure 4.47, did not show strong seeding-related trends, and generally remained within 1 cm^{-1} of the other values for all gas compositions. In contrast to shift behavior, diamond peak FWHM values did appear to show a consistent trend based on seeding density among all chemistries. All depositions showed minimum FWHM values at 2.25×10^{8} cm^{-2} (0.01% colloid) and maximum values at 1.5×10^{9} cm^{-2} (0.1% colloid). Like the diamond peak shift values, phase-purity related analysis, both integrated diamond peak areas and peak intensity ratios (shown in Figure 4.48), lacked any readily discernable trends based on areal seeding density. Average values for Raman characteristics, which are listed in Table 4.6, showed relatively little variation based on the source monomer used for deposition, with diamond peak shift values showing a total range of 0.5 cm^{-1} and a FWHM range of 1.4 cm^{-1}.

Optical emission spectroscopy measurements were previously made on plasmas of the same approximate conditions as those used for these depositions. Atomic hydrogen emission ratios (H_β/H_α and H_γ/H_α, Figures 4.26, 4.28, and 4.32) were very similar for these conditions. The relative intensities of atomic hydrogen compared to molecular hydrogen were very similar for methanol (Figure 4.29) and carbon monoxide mixtures, while the methane mixture intensities were approximately 15 - 20 % higher. Non-hydrogen constituent emissions (Figures 4.27, 4.30, and 4.33) were also quite similar among the three compositions.

As was previously mentioned, ultrasonically scratched silicon substrates were included in each of the variable seeding studies. SEM micrographs of the resultant depositions are shown in Figure 4.49. One can readily observe differences in nucleation densities on these substrates. However, these differences did not appear to be consistently related to substrate temperature or gas chemistry. Therefore, it followed that part of the difference in depositions resulted from non-uniformities in the substrate surface characteristics on the scratched substrates. The observed non-uniformities support the utility of the seeding process for the standard production of continuous films using different deposition parameters.

Discussion of Results

General Deposition Characteristics

Deposition of diamond containing films was demonstrated for a range of gas pressures, substrate temperatures and gas compositions in this ECR system. Figure 4.50 shows the plotted compositional values for the various depositions on a ternary diagram using the same style as the "Bachmann" triangle (discussed in Chapter 2). This figure shows a large separation between compositions used for very low pressure (< 100 mTorr) and higher pressure (>0.6 Torr) deposition. However, all plotted compositions fell within the approximate range established by Bachmann, et al. [Bac91], for successful diamond deposition. Gas pressure and composition appeared to have the largest effects on resultant deposition characteristics, while substrate temperature played a somewhat smaller role and microwave power over the range 1000 - 1400 W had relatively little obvious influence. OES analysis revealed that monomer species were efficiently dissociated in the ECR plasma environment at 1.0 Torr pressure and 1000 W microwave power, based on the highly similar emission behavior of secondary (i.e., formed through gas-phase reactions) non-hydrogen constituents in plasmas using different primary (source) monomers.

It is widely recognized that atomic hydrogen plays a critical role in typical diamond CVD systems. Preferential etching of non-diamond phases, stabilization of the diamond surface through the termination of dangling bonds, and abstraction of surface terminating hydrogen to create active growth sites are all key functions attributed to atomic hydrogen. Oxygen likewise provides a significant modification role in the diamond deposition process. Addition of oxygen to the deposition gas mixture, even at less than 0.5% of the total gas composition, has been shown to significantly increase the concentration of atomic hydrogen present in a microwave plasma system [Muc89]. Also, oxygen may take a direct role in the etching of non-diamond phase carbon, either in pure atomic or molecular form ($\sim 10^4$ - 10^5 times more efficient reactants with graphite than is H [Muc89}) or as part of the OH radical.

Inclusions having Raman signatures similar to polyacetylene formed a significant non-diamond constituent in films deposited in this ECR system, along with other forms of hydrogenated diamond-like and amorphous carbon. The formation of polyacetylene on the growing diamond surface has been speculated to correlate with the relative concentration of acetylene in the gas phase (in this case, where acetylene was not part of the source gas, it may be formed as a product of the plasma reaction process), as well as with a lack of sufficient atomic hydrogen production in the growth process [Mur91]. According to this theory, adsorption of acetylene (C_2H_2) on the forming diamond surface produces a dangling bond on the "free" end of the acetylene molecule to which another gas phase acetylene may attach. This in turn leaves a dangling bond for subsequent potential addition, thus leading to polymeric incorporation in the film. However, atomic hydrogen may also terminate the acetylene dangling bond, thus preventing further polymerization. Therefore, larger fractional surface termination with hydrogen (limiting the available addition sites for acetylene), lower concentration of gas-phase acetylene (limiting its impingement rate), and greater impingement of atomic hydrogen on the growth surface (to prevent polymeric addition to adsorbed acetylene) should reduce the incorporation of polyacetylene in the forming film. However, acetylene has also been proposed as a direct diamond growth precursor in opposition to the more popular methyl radical based mechanism [Spe94]. The acetylene addition mechanism is based on addition at ledge steps on the diamond surface. Therefore, it may be possible for acetylene to play a role in both diamond and non-diamond formation, depending on the local surface characteristics.

In another proposed deposition mechanism [Spe94a], aromatic hydrocarbons (of which benzene (C_6H_6) is the simplest) in the process environment tend to condense on the diamond growth surface and serve as nuclei for sp^2-bonded carbon growth unless one of two other possible processes occur. If the surface temperature is high enough, the aromatic hydrocarbon may pyrolize into smaller fragments that may then either desorb back into the gas phase or be incorporated on the surface. At lower temperatures, impinging hydrogen may hydrogenate the hydrocarbon, which may either result in diamond formation or the production of a mixed sp^2/sp^3 carbonaceous network structure. Figure 4.51 shows schematic representations of the benzene ring and a short (6 carbon atom) segment of trans-polyacetylene, illustrating the similarity of molecular structures, i.e., single hydrogen atoms bonded to each carbon atom and alternating single and double bonds between carbon atoms. Therefore, adsorption of aromatic hydrocarbons also presents a possible mechanism for polyacetylene-like non-diamond inclusion in deposited films.

OES measurements established the presence of C_2 and C_3 in the ECR plasma environment. The existence of gas-phase carbon dimers and trimers in detectable amounts may imply that acetylene and aromatic hydrocarbons may also be present in significant quantities through gas phase reactions of the methanol (or methane or carbon monoxide) source gas. Polyacetylene-like (~1450 cm^{-1} Raman signature) and amorphous or nano-crystalline diamond (~1140 and ~1240 cm^{-1} Raman features) inclusion in films deposited from similar plasmas to those characterized by OES supports this hypothesis. The increased concentration of atomic hydrogen due to oxygen addition (as determined by actinometry) correlated well with the improved Raman characteristics seen for various deposition conditions.

Pressure played a significant role in resultant deposition properties. Depositions conducted at or below 0.6 Torr showed highly defective films (as seen in SEM) with small apparent diamond peaks under Raman analysis (i.e., low relative phase purity). Raman characterization of films deposited at 1.5 Torr showed significantly stronger diamond signals than for those deposited at 1.0 Torr under otherwise similar conditions. Actinometry measurements indicated the relative atomic hydrogen concentration of 1.0 Torr plasmas tended to be lower than that of 1.5 Torr plasmas. OES also showed the relative intensity of oxygen emission increased with pressure, which also correlated well with improved deposition quality. In the operation of the ECR system, a behavior was noted such that, as pressure increased, the apparent plasma volume (estimated by the extent of the luminous discharge region) decreased. This is a common phenomenon that has also been observed in standard microwave plasma systems and is presumed to indicate the approximate volume over which microwave power is absorbed [Sha96]. Based on this observation, the average microwave power absorbed per unit volume decreases with pressure. However, the effective volume of electron cyclotron resonance does not change because it is not pressure dependent, although the effectiveness of ECR is dependent on pressure due to corresponding variation in electron mean free path lengths. Pressure also determines impingement rates and gas-phase diffusion rates (or mean free paths). One of the proposed advantages of deposition at the low pressures of this system is improved film uniformity over larger areas than higher pressure systems. Films have been deposited in this ECR system on seeded silicon substrates up to four inches in diameter at a system pressure of 1.0 Torr.

Temperature-based effects in the ECR plasma system appeared to be more subtle than pressure-related effects, although this could be attributed to the smaller relative range of variation. Diamond phase purity, as indicated by Raman analysis, showed a general tendency to increase with increasing substrate temperature. Measured shift values of the diamond Raman peak tended to be higher at lower deposition temperatures, all other factors being constant.

Film Stress

Another factor of key interest in diamond deposition is the source, nature, and magnitude of residual stresses in the film. Generally, the predominant stress contribution comes from the difference in thermal expansion between the deposited film and the substrate at the growth temperature. Figure 4.52 shows a plot of the linear thermal expansions of diamond and silicon, along with a plot of the concomitant residual stress, as a function of temperature. The expression for this stress is

$$\sigma_{th} = \frac{E_f}{(1 - \upsilon)} \int_{T_0}^{T_d} (\alpha_s - \alpha_f) dT. \qquad 4.1$$

Here $E_f/(1-\upsilon_f)$ is the biaxial Young's modulus of the film and α_s and α_f are the thermal expansion coefficients of the substrate and film, respectively. The integral is evaluated between the deposition temperature (T_d) and room temperature (T_o). Thermal expansion mismatch stress in the silicon/diamond system reaches its maximum predicted value (of ~704 MPa) around 675 °C due to the non-linear dependence of the thermal expansion coefficient on temperature. Diamond, which has a relatively low coefficient of thermal expansion, typically experiences a compressive stress on most materials, as in the case of silicon.

Coalescence of individual crystals in the formation of thin films tends to involve a concomitant generation of tensile stress in the films. This is due to the relatively high value of free surface energy as compared to the free energy of a formed grain boundary (for a typical high-angle grain boundary, $\gamma_b \simeq \frac{1}{3}\gamma_s$). The decrease in free energy $(2\gamma_s - \gamma_b)$ therefore provides a driving force for the formation of grain boundaries upon the mutual approach of two free growth surfaces. Because the crystal grains are anchored to the substrate, this force results in an intrinsic tensile stress in the film. This is known as the grain boundary relaxation model [Hof76]. An estimate of this intrinsic stress can be calculated using the equation

$$\sigma_b = \frac{E}{(1-\upsilon)}\frac{\delta}{d}. \qquad 4.2$$

The parameter d represents the average grain size and δ is the constrained relaxation of the lattice constant. δ is estimated as $(ar - r^2/2)/(2a - r)$, where a is the lattice parameter and r is the point of closest approach between two atoms. For diamond, the value of δ is taken as 0.077 nm. Figure 4.53 shows a plot of this stress versus average grain size. Because the magnitude of stress generated is inversely proportional to the grain size of the film, it is expected that high nucleation or seed densities will result in films with higher intrinsic tensile stress.

Residual thermal expansion mismatch and grain boundary relaxation represent two primary stress sources in polycrystalline diamond films. As previously mentioned, residual stress in diamond causes shifting of the characteristic diamond peak in Raman spectroscopy. While accurate quantitative measurement by Raman is relatively difficult due to crystal domain size effects and the need for suitable calibration sources, qualitative (relative) values may be deduced based on relative shifting. A common expression for approximate stress measurement based on Raman diamond peak shifting is

$$\sigma \cong 1.62\left(\frac{\mathrm{GPa}}{\mathrm{cm}^{-1}}\right) \cdot \Delta\nu, \qquad 4.3$$

where $\Delta\nu$ is the diamond peak shift offset from the unstressed value. This expression assumes there is no stress-induced reduction in the phonon mode degeneracy. Using this expression, and combining the previously calculated theoretical stress values (Figures 4.52 and 4.53), values of approximate diamond peak shift offsets were calculated and plotted in Figure 4.54. As seen in this figure, temperature dependent offsets of diamond peak shifts over the range of 550 - 750 °C experience a total approximate variation of less than 0.1 cm^{-1}. This falls within the measurement error range in this work and was therefore not expected to have direct impact on measured values. In contrast to the temperature dependent behavior, grain boundary relaxation effects for the range of sizes expected from the variable seeding densities used in this work were expected to have an observable impact on peak shift values.

Defects (such as twins or voids) and impurities also contribute significantly to the film stress. Hydrogen, as the majority constituent of the deposition environment, is typically the primary source of non-carbon impurities in CVD diamond. Incorporation of hydrogen in polycrystalline films is said to occur predominately at grain boundaries [Mcn94]. Correlations have been drawn between the incorporation of hydrogen in diamond films and incorporation of non-diamond carbon [Sha96, Wan92]. Such non-diamond impurities result in compressive stresses because diamond's high atom density does not readily incorporate impurities within its crystal structure and non-diamond-phase carbon has a lower density than diamond.

As previously stated, polyacetylene-like features make up a substantial portion of the Raman spectra from films deposited in our ECR system. Surface enhanced Raman spectroscopy has indicated that incorporated polyacetylene in diamond films may be localized in grain boundaries [Lop96]. This correlates well with the previously stated prevalence for hydrogen incorporation at grain boundaries and the concomitant trend for increased non-diamond phase carbon incorporation with hydrogen incorporation (i.e., bound hydrogen in the hydrogenated diamond-like or amorphous carbon).

Published values of intrinsic stresses for diamond films deposited on silicon have predominantly been tensile in nature [Heh96]. Using a microwave plasma system, Sharda, et al., observed a pressure dependent variation in the nature of the stresses in deposited diamond films, based on Raman spectroscopic measurement [Sha96]. In varying the operating pressure from 70 to 20 Torr using gas mixtures of 0.8% methane in hydrogen, they saw a progressive change from tensile to compressive intrinsic film stresses at lower pressures. They correlated this stress behavior with incorporated hydrogen impurity content in the film, as measured by recoil spectroscopy. Based on the observation that hydrogen dissociation decreased as system pressure decreased, they theorized that lowering of the abstraction rate of the surface terminating hydrogen caused surrounding diamond deposition to overgrow the "residual" surface hydrogen, causing incorporation and concomitant compressive stress.

Using reference Raman peak shift values measured from single crystal natural diamonds, it was found that most films deposited in the ECR system exhibited compressive intrinsic stresses. Based on the previously stated observations regarding impurity incorporation in these films, particularly as they appeared to relate to deposition temperature, i.e.

lower measured phase purity at lower temperature with concomitant increase in compressive stress, the source of the excess compressive stress was speculated to arise from these impurities.

Microstructural Control

Use of the novel electrostatic seeding process was clearly effective in controlling the areal density of particles imparted to substrate surfaces. For coverages less than 100% of the total surface area, particle layers showed very good spacial uniformity. However, the effectiveness of high density seeding (approaching 100% coverage) in controlling resultant film characteristics was disrupted by the increased presence of relatively large particles. As a result of there proportionately larger growth rates versus the average sized particles, they tended to rapidly overgrow neighboring grains very early in the deposition process, resulting in an effective decrease in the functional "nucleation" density and hence a larger average grain size and concomitant surface roughness (Figure 4.38). This phenomenon most likely also altered the grain boundary relaxation stress in these films because of the difference in the actual average grain size versus the predicted grain size based on seed density. Because the average grain size appeared to increase, the net stress due to thermal expansion differences and grain boundary interactions was expected to be more compressive in nature. However, it must be clarified that this offset was not expected to be sufficient to account for the observed peak shift values measured in this work.

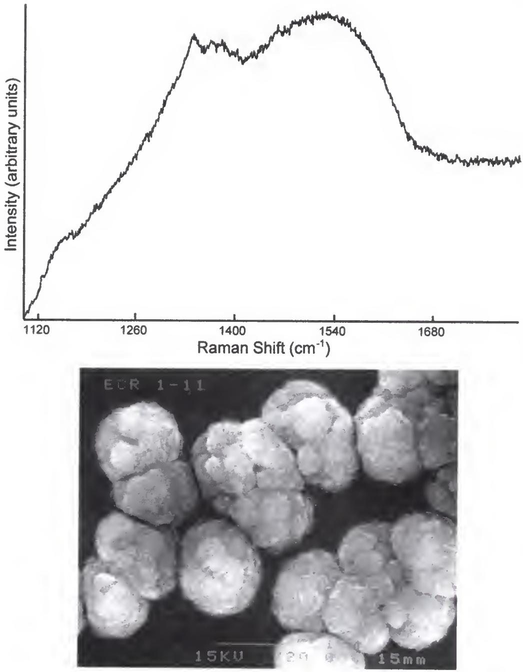

Figure 4.1 Raman spectrum and SEM taken from ECR deposited film. Process conditions were: 100% CH_3OH at 93 mTorr, 900 W microwave power, ~700 °C substrate temperature, no applied bias.

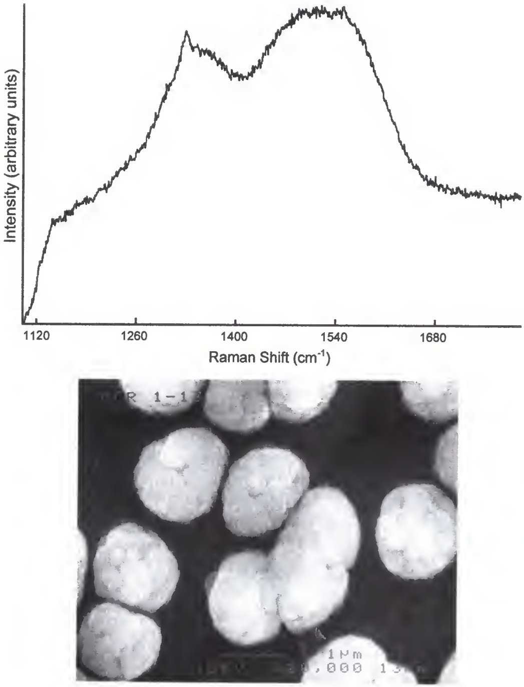

Figure 4.2 Raman spectrum and SEM taken from ECR deposited film. Process conditions were: 100% CH_3OH at 90 mTorr, 900 W microwave power, ~700 °C substrate temperature, +50 V bias.

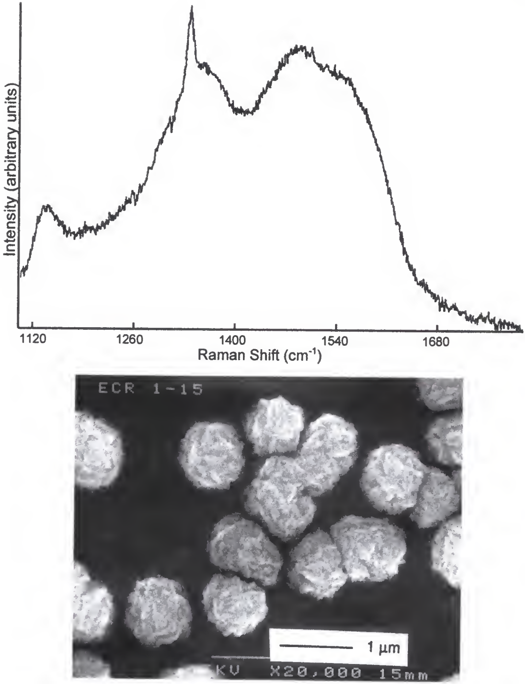

Figure 4.3 Raman spectrum and SEM taken from ECR deposited film. Process conditions were: 83% CH_3OH/17% H_2O at 96 mTorr, 900 W microwave power, ~700 °C substrate temperature, +50 V bias.

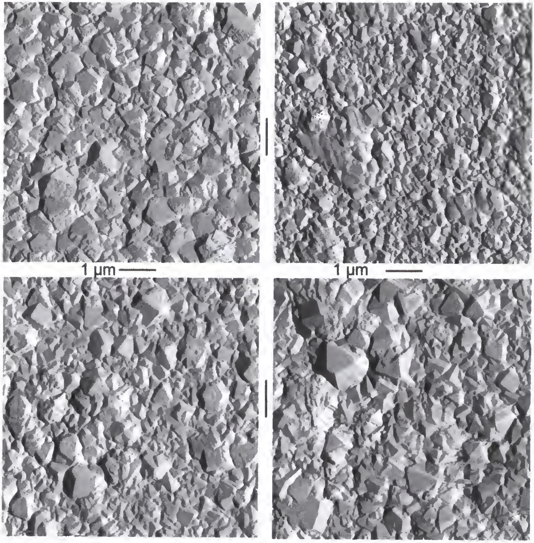

Figure 4.4 AFM micrographs of films deposited at (a) 0.6, (b) 1.0, (c) 1.5, and (d) 1.9 Torr from 1.2% methanol in hydrogen with 1000 W microwave power at 700°C.

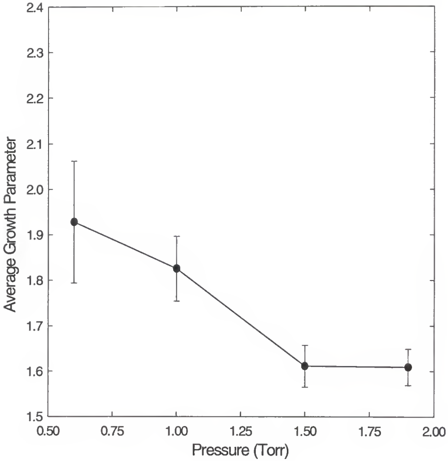

Figure 4.5 Average growth parameters versus pressure for 1.2% methanol in hydrogen at 1000 W microwave power and 700°C.

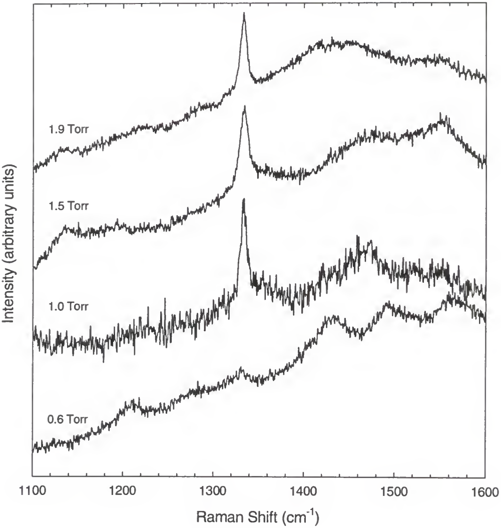

Figure 4.6 Raman spectra of films deposited at various pressures from 1.2% methanol in hydrogen at 700 ° using 1000 W microwave power.

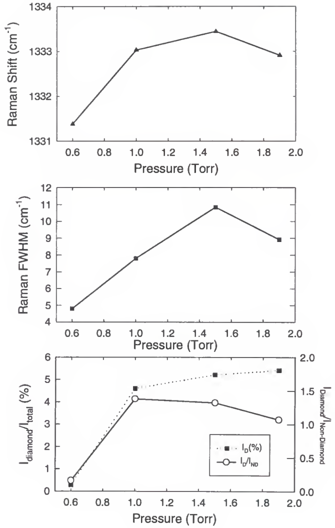

Figure 4.7 Raman values of diamond peak-shift position, full-width-at-half-maximum (FWHM), and percent integrated area of diamond peak for films deposited from 1.2% methanol at 700 °C using 1000 W microwave power.

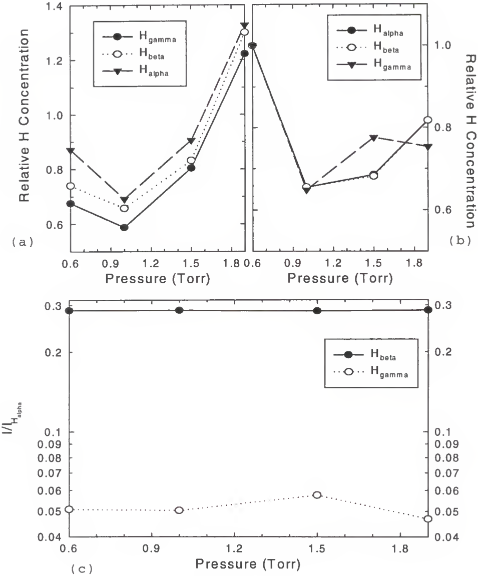

Figure 4.8 Normalized atomic hydrogen concentration as determined by actinometry measurement (a) relative to pure hydrogen at the same pressure and (b) versus pressure (normalized by 0.6 Torr value) and (c) hydrogen beta and gamma emissions relative to the alpha emission at different pressures with 1.2% methanol using 1000 W microwave power.

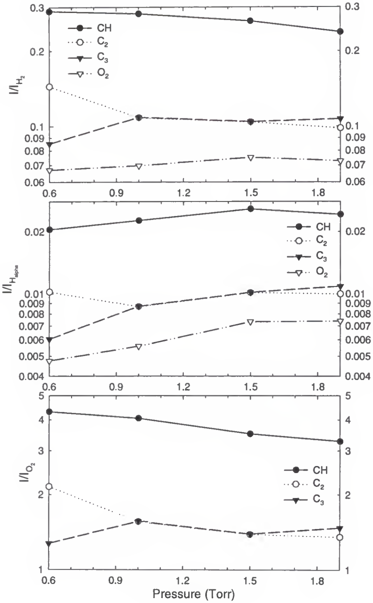

Figure 4.9 Optical emission intensities (normalized by molecular and atomic hydrogen and oxygen emission) of various non-hydrogen constituents of plasmas formed from 1.2% methanol in hydrogen using 1000 W microwave power and different pressures.

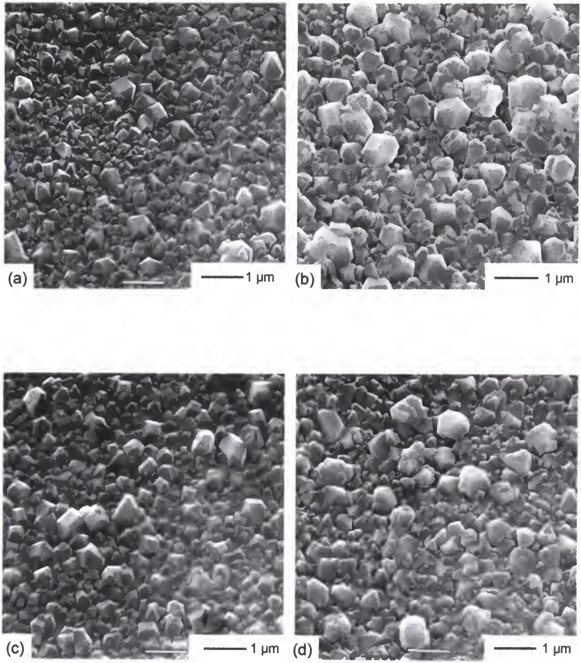

Figure 4.10 SEM micrographs of films deposited at (a) 550, (b) 600, (c) 700, and (d) 750 °C from 1.2% methanol in hydrogen at 1.0 Torr pressure using 1000 W microwave power.

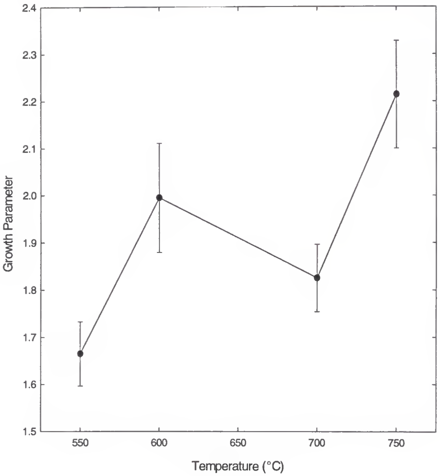

Figure 4.11 Growth parameters for films deposited at various temperatures from 1.2% methanol in hydrogen at 1.0 Torr using 1000 W microwave power.

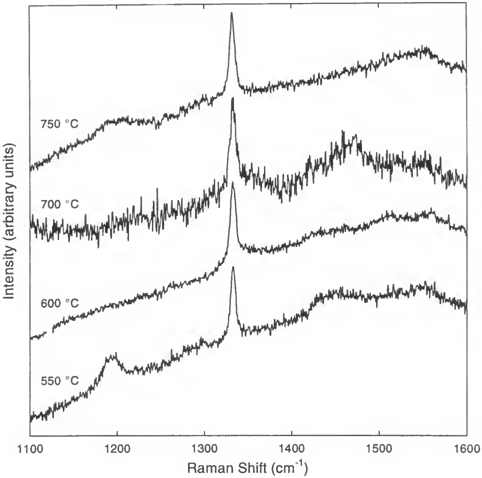

Figure 4.12 Raman spectra from films deposited at various temperatures from 1.2% methanol in hydrogen at 1.0 Torr using 1000 W microwave power.

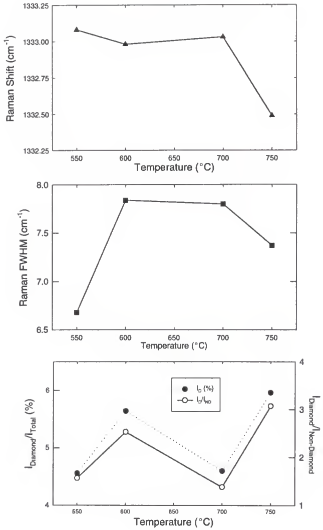

Figure 4.13 Raman analytical statistics of diamond peak position, FWHM, and diamond integrated intensity for films deposited from 1.2% methanol in hydrogen at 1.0 Torr using 1000 W microwave power.

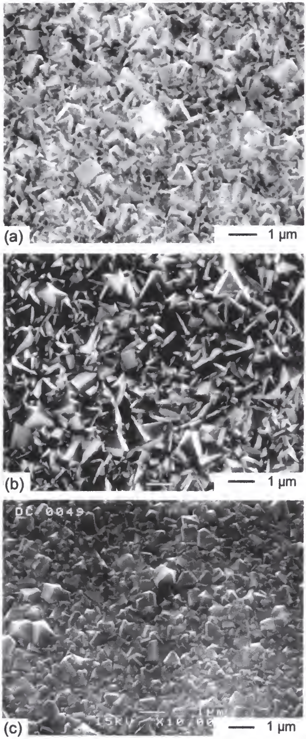

Figure 4.14 SEM micrographs of films deposited from 1.0% methanol in hydrogen at 1.0 Torr and substrate temperature of 700 °C using (a) 1000, (b) 1200, and (c) 1400 W microwave power.

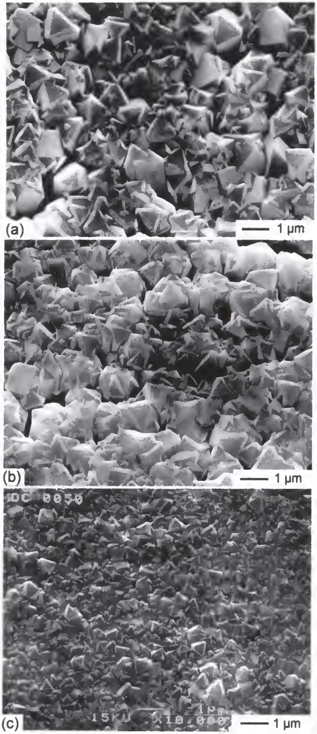

Figure 4.15 SEM micrographs of films deposited from 1.0% methanol in hydrogen at 1.5 Torr and substrate temperature of 700 °C using (a) 1000, (b) 1200, and (c) 1400 W microwave power.

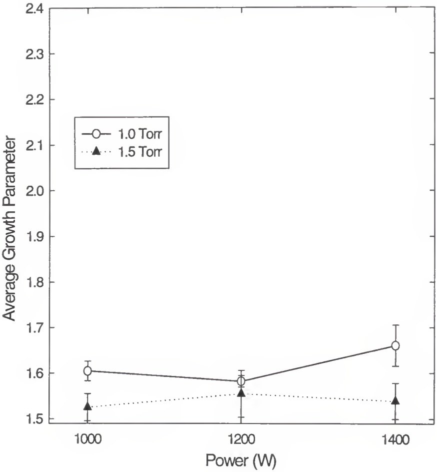

Figure 4.16 Average measured growth parameters for depositions using 1.0% methanol in hydrogen at 700 °C.

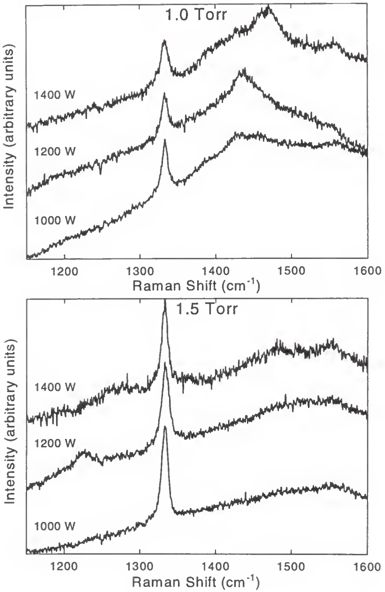

Figure 4.17 Raman spectra from films deposited on silicon at 700 °C and various microwave powers using 1.0% methanol in hydrogen.

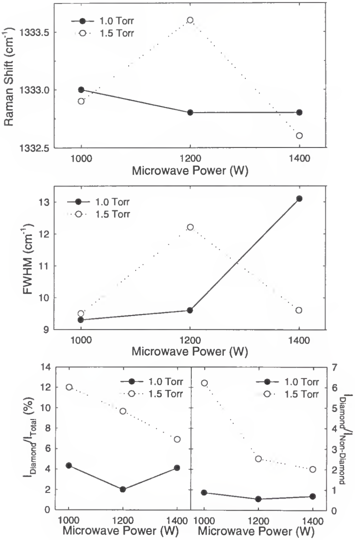

Figure 4.18 Raman characteristics for depositions on silicon at 700 °C using 1.0% methanol in hydrogen.

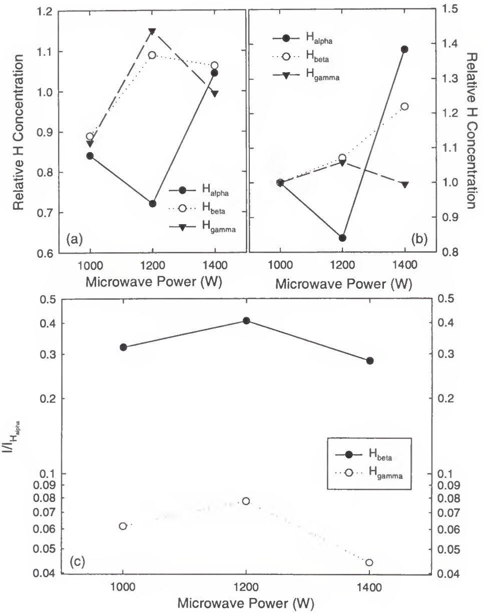

Figure 4.19 Hydrogen related OES characteristics at 1.0 Torr and 1.0% CH_3OH of (a) H concentration relative to pure hydrogen plasma at same condition, (b) H concentration relative to 1000 W condition, and (c) EEDF behavior at various powers.

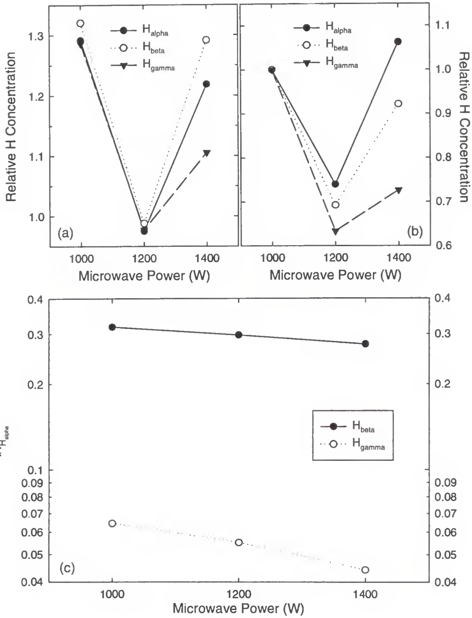

Figure 4.20 Hydrogen related OES characteristics at 1.5 Torr and 1.0% CH_3OH of (a) H concentration relative to pure hydrogen plasma at same condition, (b) H concentration relative to 1000 W condition, and (c) EEDF behavior at various powers.

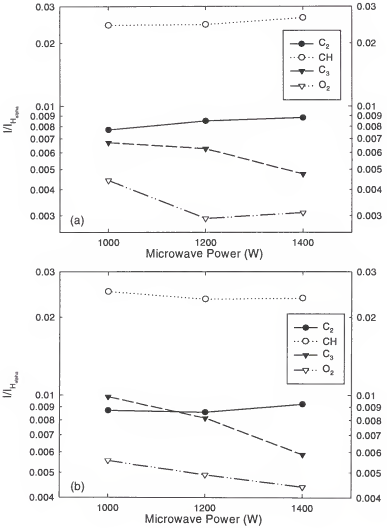

Figure 4.21 OES behavior of various non-hydrogen plasma components at several input microwave powers and pressures of (a) 1.0 and (b) 1.5 Torr.

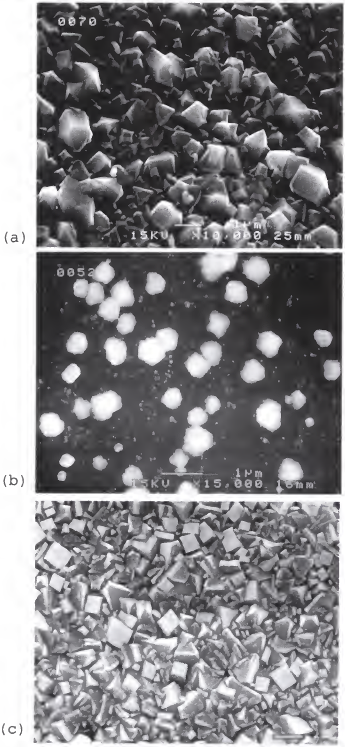

Figure 4.22 SEM micrographs of films deposited at total pressure of 1.0 Torr and (a) 1.0% CH_4, 700 °C, 1000 W, (b) 1.0% CH_4, 0.5% O_2, 700 °C, 1400 W, and (c) 0.5% CH_4, 1.0% CH_3OH, 700 °C, 1000 W.

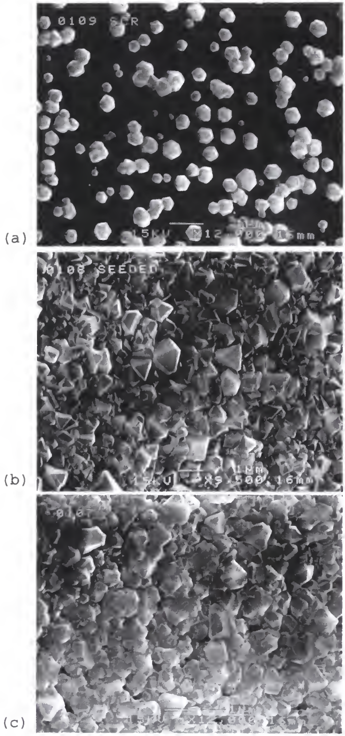

Figure 4.23 SEM micrographs of films deposited at total pressure of 1.5 Torr, 1000 W and (a) 1.0% CH_4, 750 °C, (b) 1.5% CH_4, 0.4% O_2, 750 °C, and (c) 1.0% CH_4, 0.4% O_2, 700 °C.

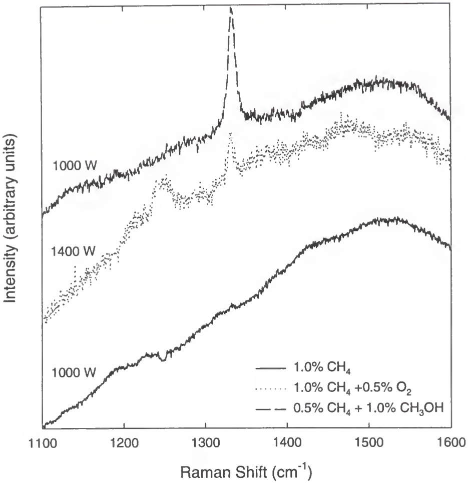

Figure 4.24 Raman spectra for films shown in Figure 4.23.

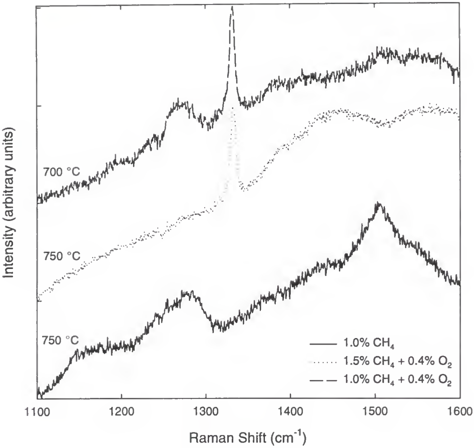

Figure 4.25 Raman spectra for films shown in Figure 4.24.

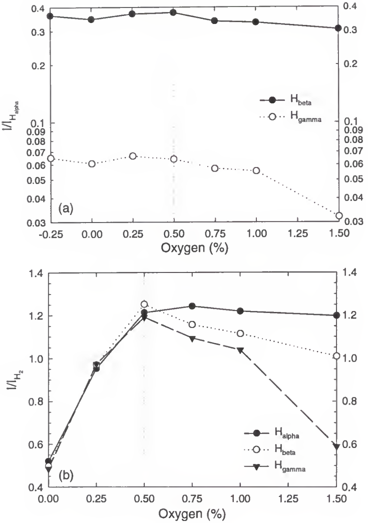

Figure 4.26 OES of methane/oxygen mixtures in hydrogen. (a) Atomic hydrogen ratios indicating EEDF behavior and (b) intensities of atomic hydrogen (relative to molecular hydrogen emission), normalized by the value for pure hydrogen. (Dotted line indicates C/O = 1.)

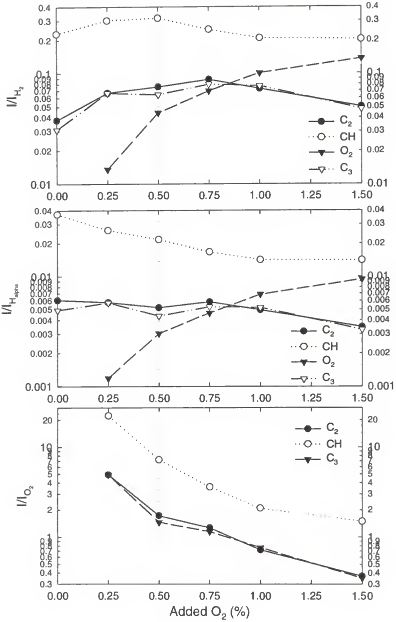

Figure 4.27 Emission intensities (relative to atomic and molecular hydrogen and oxygen emissions) of various plasma constituents in a 1.0% methane plasma with added oxygen. (Dotted line indicates C/O = 1.)

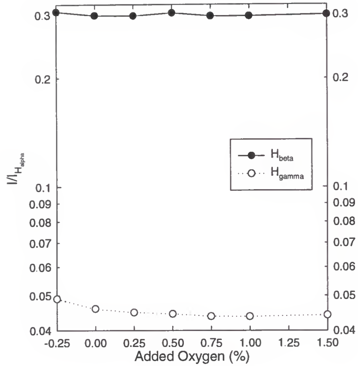

Figure 4.28 Atomic hydrogen emission ratios for 1.0% methanol/hydrogen mixtures with added oxygen.

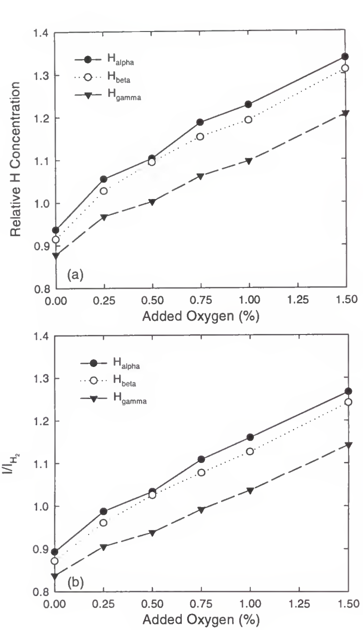

Figure 4.29 Plots of (a) hydrogen concentration (as determined by argon actinometry) relative to pure hydrogen and (b) hydrogen emission intensities relative to molecular hydrogen emission, normalized by the value for pure hydrogen for mixtures of 1.0% methanol and oxygen in hydrogen.

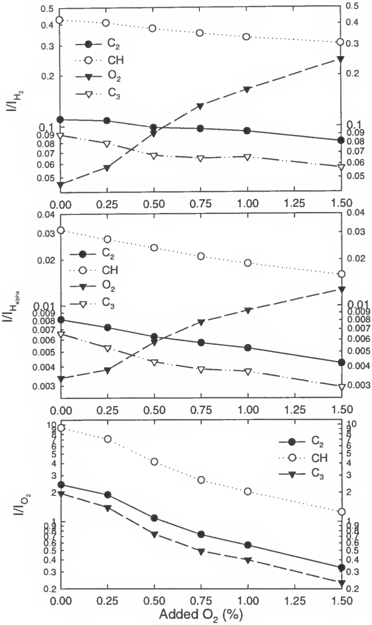

Figure 4.30 OES intensities of various non-hydrogen plasma constituents in a 1.0% methanol plasma plotted relative to molecular and atomic hydrogen, and oxygen emission intensities for various amounts of added O_2.

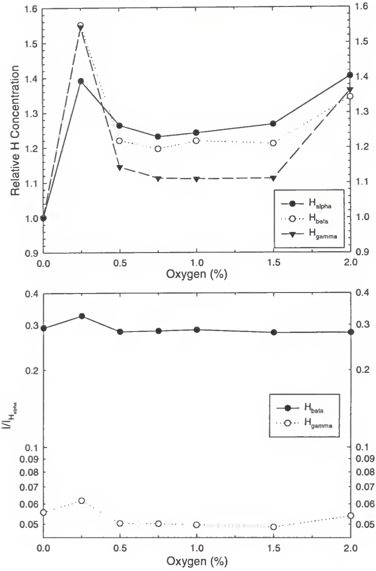

Figure 4.31 Plots of relative atomic hydrogen concentration and atomic hydrogen emission ratios for hydrogen plasmas with added oxygen.

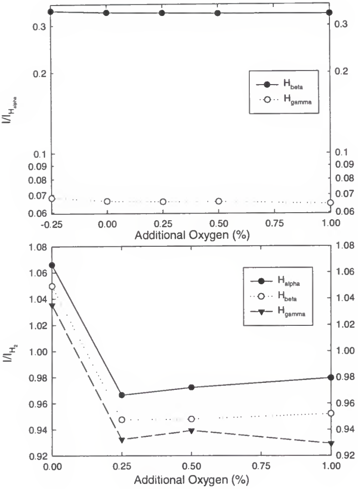

Figure 4.32 OES of carbon monoxide/oxygen mixtures in hydrogen. (a) Atomic hydrogen ratios indicating EEDF behavior and (b) intensities of atomic hydrogen (relative to molecular hydrogen emission), normalized by the value for pure hydrogen.

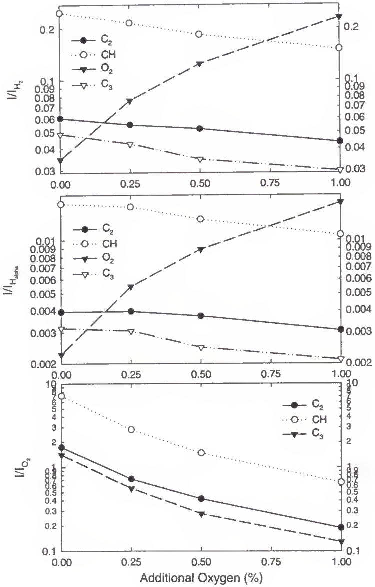

Figure 4.33 Emission intensities (relative to atomic and molecular hydrogen and oxygen emissions) of various plasma constituents in a 1.0% carbon monoxide plasma with added oxygen.

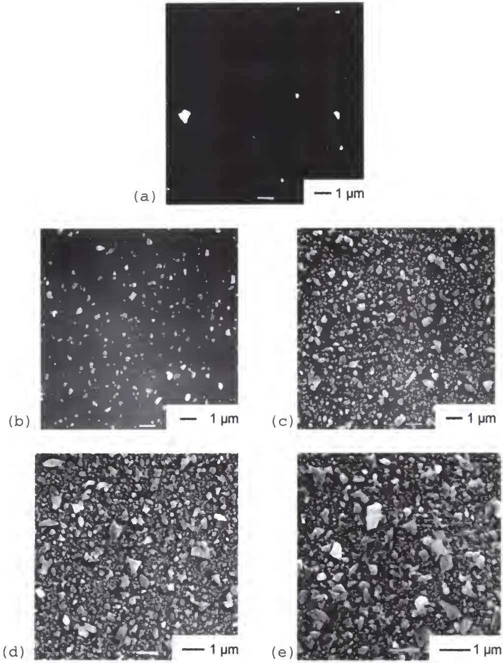

Figure 4.34 SEM micrographs of diamond particle seed layers created using (a) 0.001, (b) 0.01, (c) 0.1, (d) 1.0, and (e) 10.0% diamond colloidal suspensions.

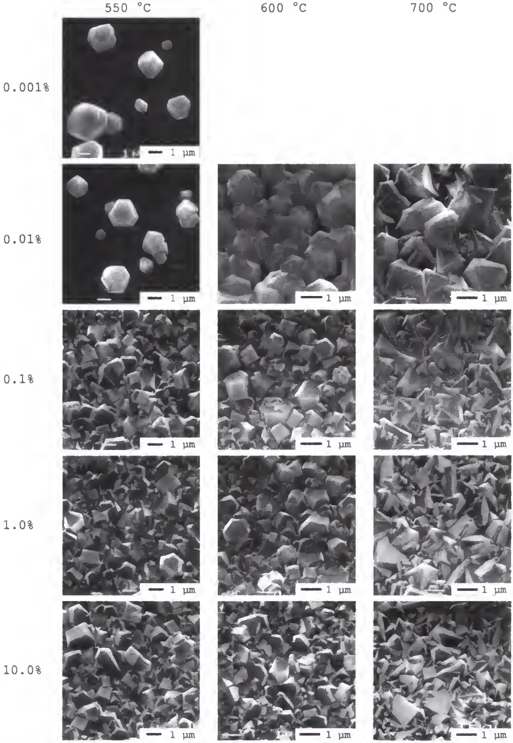

Figure 4.35 SEM micrographs of resultant deposits on the stated colloid seeded substrates at the listed temperatures from 1.0% methanol in hydrogen at 1.0 Torr using 1000 W microwave power.

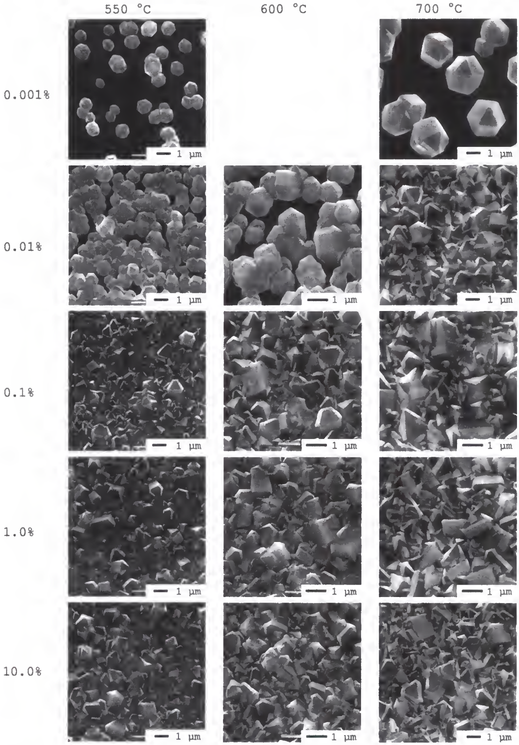

Figure 4.36 SEM micrographs of resultant deposits on the stated colloid seeded substrates at the listed temperatures from 1.0% methanol/0.25% oxygen mixtures in hydrogen at 1.0 Torr using 1000 W microwave power.

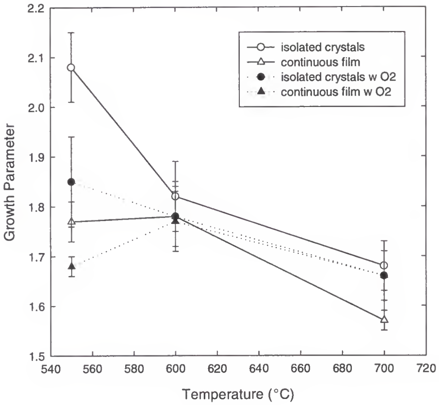

Figure 4.37 Plotted values of the measured growth parameter for films and isolated crystals deposited at various temperatures on variably seeded silicon substrates from 1.0% methanol with and without 0.25% added oxygen in hydrogen using 1000 W microwave power and 1.0 Torr total pressure.

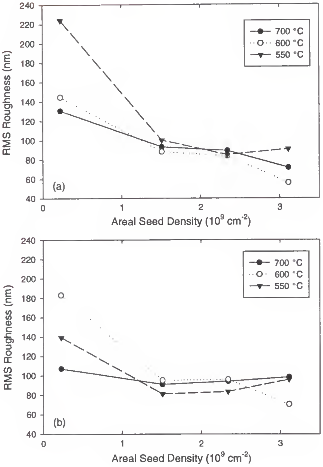

Figure 4.38 AFM measured RMS roughness values for films deposited from different areal seed densities using 1.0% methanol (a) without and (b) with 0.25% oxygen at 1.0 Torr using 1000 W microwave power.

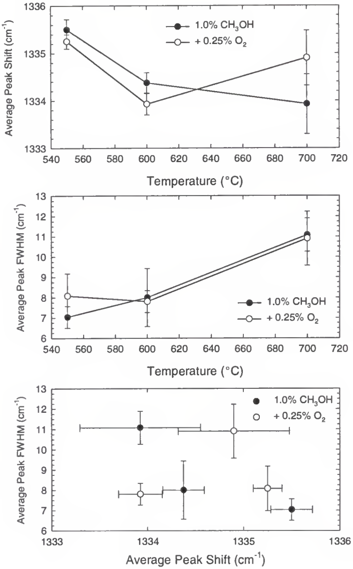

Figure 4.39 Averaged Raman characteristics of diamond peak shift and FWHM for films deposited on variably seeded substrates from methanol/oxygen/hydrogen gas mixtures at 1.0 Torr using 1000 W microwave power.

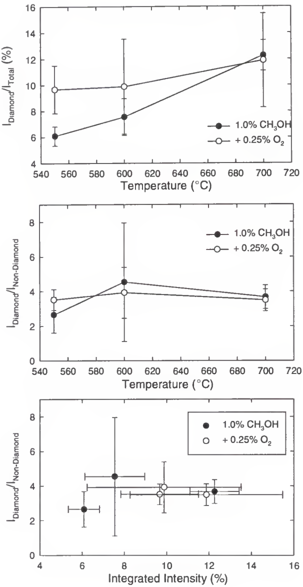

Figure 4.40 Averaged values of Raman integrated diamond peak areas and peak intensity ratios for films deposited on variably seeded substrates from methanol/oxygen/hydrogen gas mixtures at 1.0 Torr using 1000 W microwave power.

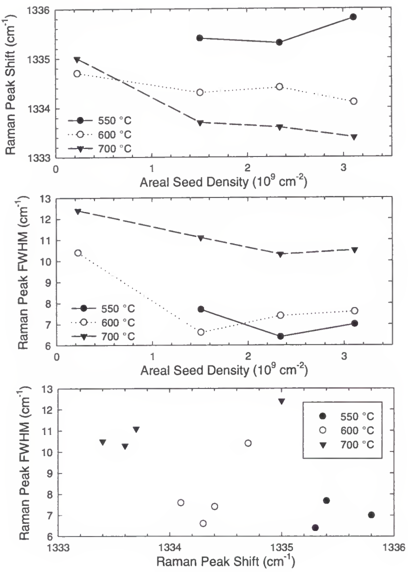

Figure 4.41 Raman diamond peak shifts and widths from films deposited from 1.0% methanol in hydrogen at 1.0 Torr using 1000 W microwave power and variable areal seed densities.

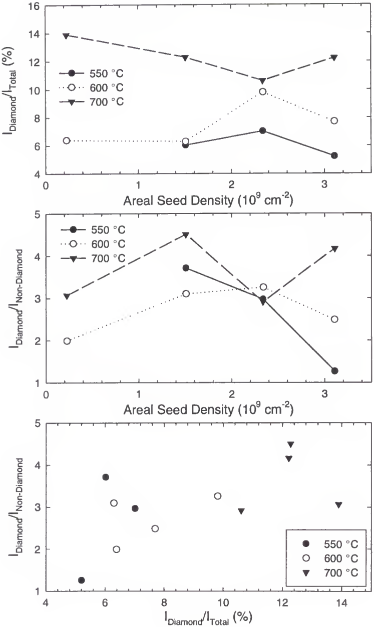

Figure 4.42 Raman integrated diamond peak areas and peak intensity ratios for films deposited on variably seeded substrates from 1.0% methanol in hydrogen gas mixtures at 1.0 Torr using 1000 W microwave power.

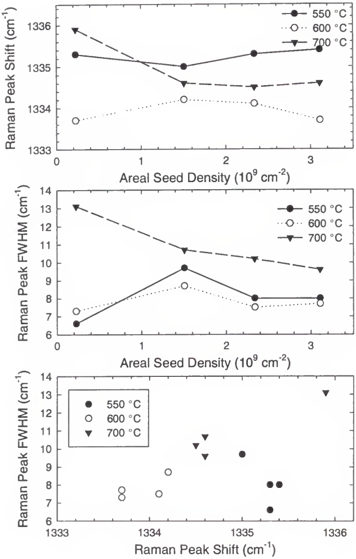

Figure 4.43 Raman diamond peak shifts and widths from films deposited from 1.0% methanol and 0.25% oxygen in hydrogen at 1.0 Torr using 1000 W microwave power and variable areal seed densities.

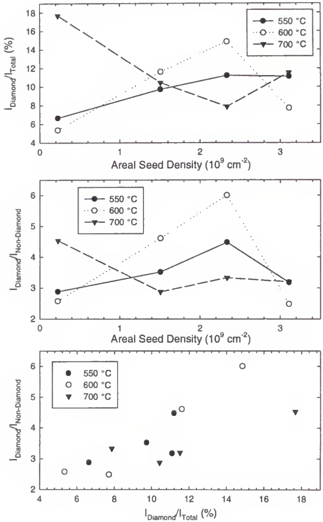

Figure 4.44 Raman integrated diamond peak areas and peak intensity ratios for films deposited on variably seeded substrates from 1.0% methanol and 0.25% oxygen in hydrogen gas mixtures at 1.0 Torr using 1000 W microwave power.

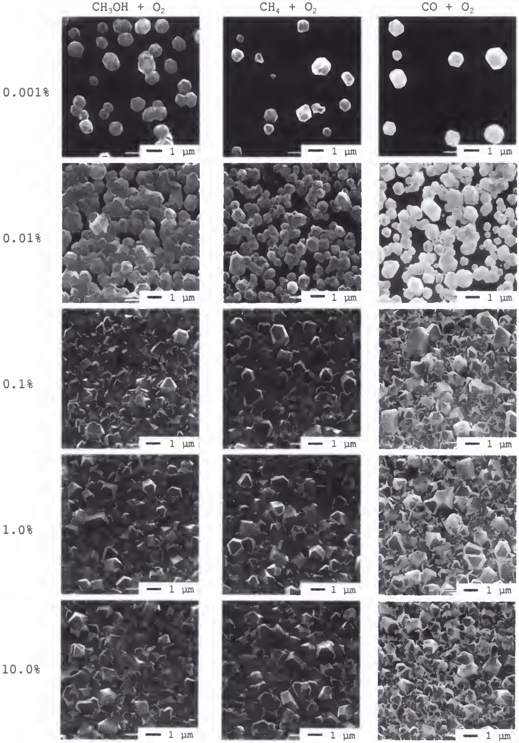

Figure 4.45 SEM micrographs of resultant deposits on the stated colloid seeded substrates at 550 °C from methanol, methane, and carbon monoxide gas mixtures (with equivalent C/H/O ratios) in hydrogen at 1.0 Torr using 1000 W microwave power.

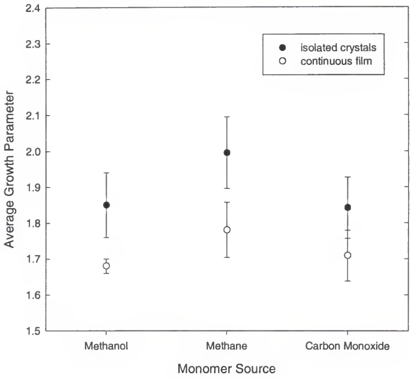

Figure 4.46 Average measured growth parameters for continuous films and isolated crystals deposited on variably seeded silicon substrates at 550 °C from different monomer sources maintaining the same C/H/O feed ratios at 1.0 Torr using 1000 W microwave power.

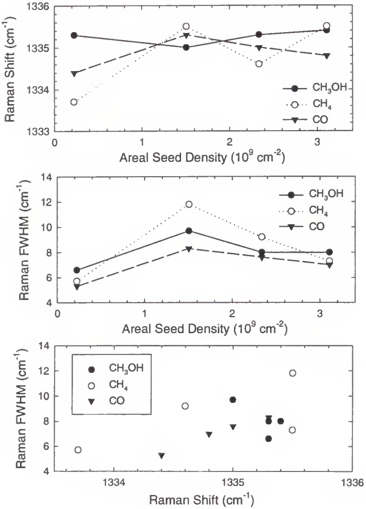

Figure 4.47 Raman characteristics of diamond peak position and FWHM for films deposited on variably seeded silicon substrates at 550 °C from different monomer sources maintaining the same C/H/O feed ratios.

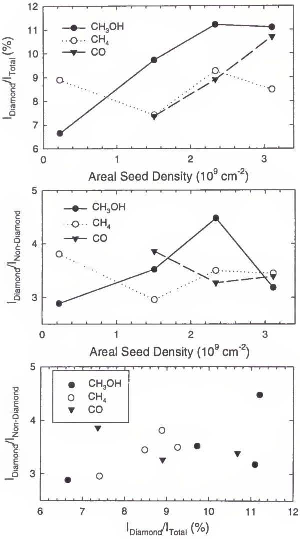

Figure 4.48 Raman characteristics of diamond peak percentage area and peak intensity relative to non-diamond for films deposited on variably seeded silicon substrates at 550 °C from different monomer sources maintaining the same C/H/O feed ratios.

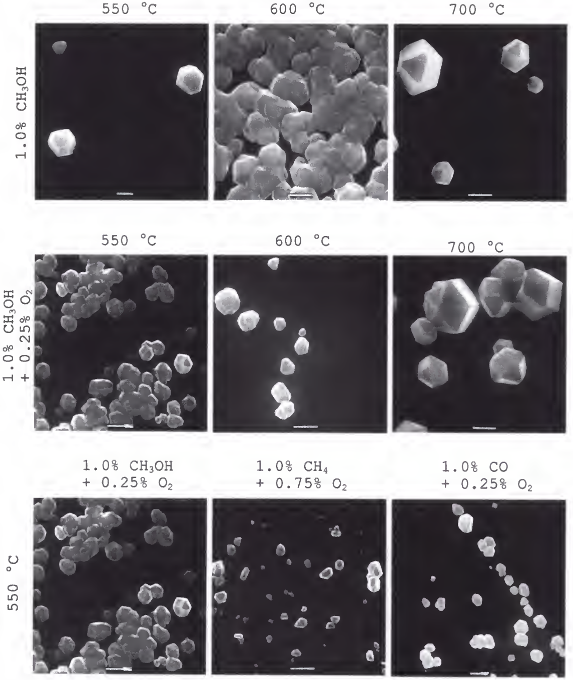
550 °C
600 °C
700 °C
1.0% CH_3OH
550 °C
600 °C
700 °C
1.0% CH_3OH + 0.25% O_2
1.0% CH_3OH + 0.25% O_2
1.0% CH_4 + 0.75% O_2
1.0% CO + 0.25% O_2
550 °C

Figure 4.49 SEM micrographs of resultant deposition on scratched silicon substrates at the stated temperatures and gas compositions at 1.0 Torr using 1000 W microwave power.

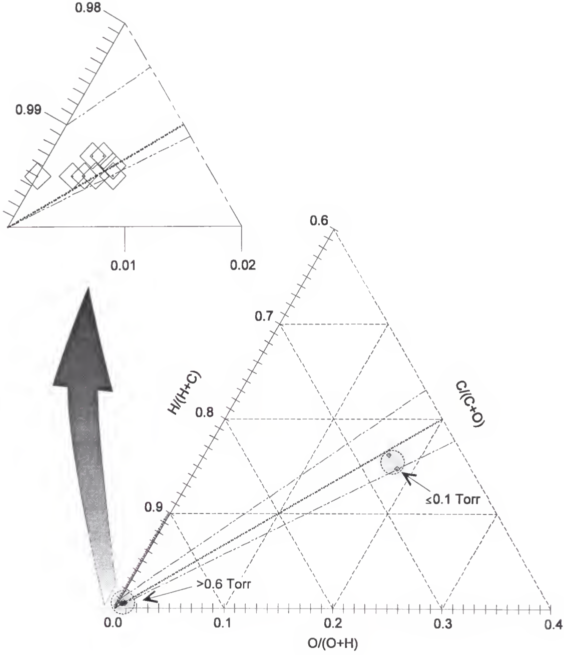

Figure 4.50 Ternary compositional plots showing the relative quantities of carbon, oxygen, and hydrogen used for diamond deposition in the ECR system for this work.

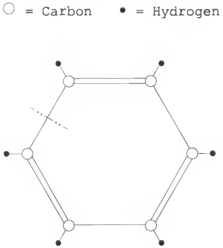

Benzene

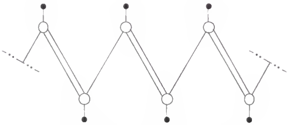

Trans-Polyacetylene

Figure 4.51 Schematic representations of benzene and trans-polyacetylene molecular structures.

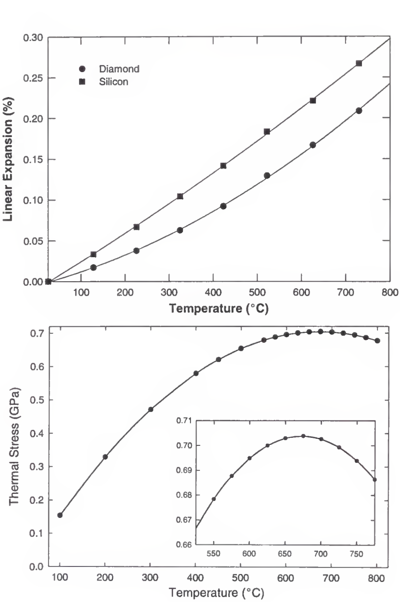

Figure 4.52 Temperature dependent linear thermal expansion values for silicon and diamond and approximate residual compressive stress values.

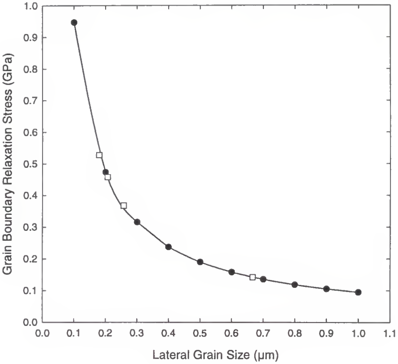

Figure 4.53 Theoretical tensile stress values for diamond as a function of average lateral grain size. Open squares represent values for seed particle separation distances used in this work.

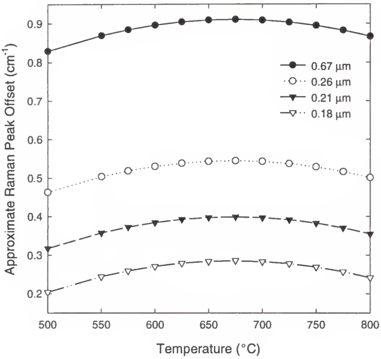

Figure 4.54 Approximate relative values of Raman diamond peak shift based on deposition temperature on silicon and different average diamond grain size.

CHAPTER 5
CONCLUSIONS

The objective of this work was to establish the deposition characteristics of a custom electron cyclotron resonance enhanced microwave plasma system for diamond coatings, based on the variation of fundamental system parameters of gas pressure, substrate temperature, microwave power, and source-gas composition. Having established these general guidelines, experimental work was performed with the intent of establishing a method of effectively controlled nucleation density through the application of diamond particle seeding that would be relatively insensitive to specific deposition conditions. Using this process, the sensitivity of diamond film characteristics based on the areal density of these seed "nuclei" were investigated. The following conclusions were made in regard to the completion of these stated objectives.

System Dependant Deposition Characteristics

Parameters of gas pressure, composition and microwave power affected diamond deposition characteristics primarily through the alteration of the plasma chemistry, with pressure and composition being the most critical factors within the investigated conditions. Optical emission spectroscopy, through the use of actinometry, was effective in showing changes in relative atomic hydrogen concentrations based on each of these parameters, as well as detecting changes in the electron energy distribution function. According to OES measurements, the ECR-enhanced plasma efficiently dissociated feed gases to form secondary gas species of CH, C_2, C_3, and O_2 under the conditions investigated, regardless of the specific source monomer used. Observed substrate-temperature related effects over the range investigated (550 - 750 °C) were less pronounced than gas-related parameters. Surface reaction and diffusion rates and fractional surface coverage by hydrogen were the most likely factors affected by temperature. For this ECR-enhanced plasma system, the production of secondary gas-phase monomers (such as carbon dimers, trimers, and possibly aromatic hydrocarbons such as benzene) resulted in films containing significant fractions of non-diamond phase carbon, including forms of hydrogenated diamond-like-carbon and possibly polyacetylene. Raman analysis of deposited films indicated the prevalent formation of compressive intrinsic growth stresses, which correlated well with the speculated incorporation of impurity species and phases.

Controlled Areal Seeding

Over the course of this research, several methods were investigated for the enhanced and controlled nucleation of diamond. The result of this was the development of a novel seeding technique utilizing a thin polymer layer to modify the surface charge of silicon, thus providing an electrostatic force favorable to the deposition of diamond particles from an aqueous colloid. When combined with a spin coating procedure, particle seed layers exhibiting excellent areal uniformities over areas greater than 2" in diameter were achieved.

Quantities such as phase purity, stress, and crystalline quality, as determined by Raman analysis, showed little consistent dependence on the areal density of seeding over the ranges investigated. Expected grain boundary effects were apparently disrupted by seed particle size variation and impurity incorporation. Morphological variance in the form of surface roughness showed measurable dependence on areal seed density, with lower densities exhibiting higher roughnesses due to higher average grain sizes, although particle size variation once again caused deviation from theoretically predicted results.

LIST OF REFERENCES

Age91 J. W. Ager, D. K. Veirs and G. M. Rosenblatt, *Phys. Rev. B* 43, 6491 (1991)

Age93 J. W. Ager and M. D. Drory, *Phys. Rev. B* 48, 2601 (1993)

Ama89 G. Amaratunga, A. Putnis, K. Clay, and W. Milne, *Appl. Phys. Lett.* 55, 634 (1989)

Ang68 J. C. Angus, H. A. Will and W. S. Stanko, *J. Appl. Phys.* 39, 2915 (1968)

Ang95 J. C. Angus, W. D. Cassidy, L. Wang, Y. Wang, E. Evans, C. S. Kovach and M. A. Tamor, Mat. Res. Soc. Symp. Proc. 383, 45 (1995)

Asm90 J. Asmussen, in *Handbook of Plasma Processing Technology*, S. M. Rossnagel, J. J. Cuomo, and W. D. Westwood Eds., Noyes Publications, Park Ridge, NJ, p. 293 (1990)

Bac91 P. Bachmann, D. Leers, and H. Lydtin, *Diam. Rel. Mater.* 1, 1 (1991)

Bai92 Y. Baik and K. Y. Eun, *Thin Solid Films* 214, 123 (1992)

Bal93 G. Balestrino, M. Marinelli, E. Milani, A. Paoletti, I. Pinter, A. Tebano, and P. Paroli, *Appl. Phys. Lett.* 62, 879 (1993)

Bar89 Y. Bar-Yam, T. D. Moustakas, *Nature* 342, 786 (1989)

Bar94 S. Barrat, I. Dieguez, H. Michel, and E. Bauer-Grosse, *Diam. Rel. Mater.* 3, 520 (1994)

Bel91 D. N. Belton and S. J. Schmieg, *J. Appl. Phys.* 69, 3032 (1991)

Ber95 L. Bergman and R. J. Nemanich, *J. Appl. Phys.* 78, 6709 (1995)

Ber97 L. Bergman and R. J. Nemanich, in: *Handbook of Optical Properties Vol. II*, (R. E. Hummel and P. WiBmann eds.), CRC Press, Boca Raton, 331 (1997)

Bou91 P. Bou and L. Vandenbulcke, *J. Electrochem. Soc.* 138, 2991 (1991)

Car97 M. L. Carasso, J. H. Adair, P. A. Demkowicz, D. R. Gilbert, and R. K. Singh, *SPIE Proceedings* Vol. 3060, 203-12 (1997)

Cha88 C. P. Chang, D. L. Flamm, D. E. Ibbotson, and J. A. Mucha, *J. Appl. Phys.* 63, 1744 (1988)

Cha92 J. J. Chang and T. D. Mantei, *J. Appl. Phys.* 71, 5724 (1992)

Che95 C. J. Chen, L. Chang, T. S. Lin, and F. R. Chen, *J. Mater. Res.* 10, 3041 (1995)

Chu90 C. J. Chu, M. P. D'Evelyn, R. H. Hauge, and J. L. Margrave, *J. Mater. Res.* 5, 2405 (1990)

Cob80 J. W. Coburn and M. Chen, *J. Appl. Phys.* 51, 3134 (1980)

Dev92 M. P. D'Evelyn, C. J. Chu, R. H. Hauge and J. L. Margrave, *J. Appl. Phys.* 71, 1528 (1992)

Edd93 C. R. Eddy, D. L. Youchison and B. D. Sartwell, *Diam. Rel. Mater.* 3, 105 (1993)

Eve62 W. G. Eversole, U.S. Patent No. 3,030,187 (1962)

Fay94 L. Fayette, M. Mermoux, and B. Marcus, *Diam. Rel. Mater.* 3, 480 (1994)

Fre89 M. Frenklach, *J. Appl. Phys.* 65, 5142 (1989)

Fre91 M. Frenklach, in: *Diamond and Diamond-Like Films and Coatings*, (R. E. Clausing ed.), Plenum Press, NY, 499, (1991)

Ger94 J. Gerber, M. Weiler, O. Sohr, K. Jung, and H.

Ehrardt, *Diam. Rel. Mater.* 3, 506 (1994)

Gil97a D. R. Gilbert, R. Singh, R. Clarke, and S. Murugkar, Appl. Phys. Lett. 70, 1974 (1997)

Gil97b D. R. Gilbert, M. L. Carasso, P. A. Demkowicz, R. K. Singh, and J. H. Adair, *J. Electron. Mater.* 26, 1326 (1997)

Gom93 C. Gomez-Aleixandre, O. Sanchez, A. Castro, and J. M. Albella, *J. Appl. Phys.* 74, 3752 (1993)

Gru94 D. M. Gruen, S. Liu, A. R. Krauss, and X. Pan, *J. Appl. Phys.* 75, 1758 (1994)

Har94 S. J. Harris and A. M. Weiner, *J. Appl. Phys.* 75, 5026 (1994)

Heh96 L. P. Hehn, *Fracture and Residual Stress Measurement in Polycrystalline CVD Diamond*, Doctoral Dissertation, Department of Materials Science and Engineering, University of Florida, p. 34 (1996)

Hir90 A. Hiraki, H. Kawarada, J. Wei, J. S. Ma, and J. Suzuki, SPIE Vol. 1325, 73 (1990)

Hof76 R. W. Hoffman, *Thin Solid Films* 34, 185 (1976)

Jin93 S. Jin and T. D. Moustakas, Mat. Res. Soc. Symp. Proc. Vol. 280, 701 (1993)

Jin94 S. Jin, M. Fanciulli, and T. D. Moustakas, Diam. Rel. Mater. 3, 878 (1994)

Kad93 M. Kadano, T. Inoue, A. Miyanaga, and S. Yamazaki, Jpn. J. Appl. Phys 32, 3231 (1993)

Kaw87 H. Kawarada, K. S. Mar, and A. Hiraki, *Jpn. J. Appl. Phys.* 26, L1032 (1987)

Kim92 J. W. Kim, Y. Baik, K. Y. Eun, and D. N. Yoon, *Thin Solid Films* 212, 104 (1992)

Kom93 M. Komori, T. Maki, T. Kim, G. L. Hou, Y. Sakaguchi, K. Sakuta, and T. Kobayashi, *Appl. Phys. Lett.* 62, 582 (1993)

Lax50 B. Lax, W. P. Allis, and S. C. Brown, *J. Appl. Phys.* 21, 1297 (1950)

Lee97 D. G. Lee and R. K. Singh, *Appl. Phys. Lett.* 70, 1542 (1997)

Lid90 D. R. Lide, CRC Handbook of Chemistry and Physics, 71st Edition, 10-41 (1990)

Lop96 T. Lopez-Rios, E. Sandre, S. Leclercq, and E. Sauvain, *Phys. Rev. Lett.* 76, 4935 (1996)

Mae95 H. Maeda, K. Ohtsubo, M. Irie, N. Ohya, K. Kusakabe, and S. Morooka, *J. Mater. Res.* 10, 3115 (1995)

Mak96 H. Makita, K. Nishimura, N. Jiang, A. Hatta, T. Ito, A. Hiraki, *Thin Solid Films* 281, 279 (1996)

Man96 T. D. Mantei, Z. Ring, M. Schweizer, and H. E. Jackson, *Jpn. J. Appl. Phys.* 35, 2516 (1996)

Mar96 N. Marechal and S. Yamashita, *Thin Solid Films* 290-291, 131 (1996)

Mas91 A. Masood, M. Aslam, M. A. Tamor, and T. J. Potter, *J. Electrochem. Soc.* 138, L67 (1991)

May94 P. W. May, C. A. Rego, C. G. Trevor, E. C. Williamson, M. N. R. Ashfold, K. N. Rosser, and N. M. Everitt, *Diam. Rel. Mater.* 3, 1375 (1994)

Mcn94 K. M. McNamara, K. K. Gleason, *Chem. Mater.* 6, 39 (1994)

Meh90 S. P. Mehandru and A. B. Anderson, *J. Mater. Res.* 5, 2286 (1990)

Muc89 J. A. Mucha, D. L. Flamm, and D. E. Ibbotson, *J. Appl. Phys.* 65, 3448 (1989)

Mur90 Y. Muranaka, H. Yamashita, K. Sato, and H. Miyadera, *J. Appl. Phys.* 67, 6247 (1990)

Mur91 Y. Muranaka, H. Yamashita, and H. Miyadera, *J. Vac. Sci. Technol. A* 9, 76 (1990)

Mur94 Y. Muranaka, H. Yamashita and H. Miyadera, *Diam.*

Rel. Mater. 3, 313 (1994)

Mur96 A. Murai, I. Ohya, T. Yasui, H. Tahara, and T. Yoshikawa, *Thin Solid Films* 281-282, 146 (1996)

Nak90 S. Nakao and S. Maruno, *J. Crystal Growth* 99, 1215 (1990)

Nar92 J. Narayan, V. P. Godbole, G. Matera, *J. Appl. Phys.* 71, 966 (1992)

Nas93 K. Nassau, in: *Diamond Films and Coatings*, (R. F. Davis ed.), Noyes Publications, NJ, 40-55, (1993)

Oht90 N. Ohtake and M. Yoshikawa, *J. Electrochem. Soc.* 137, 717 (1990)

Oji93 S. Ojika, S. Yamashita, K. Kataoka, T. Ishikura, A. Yamaguchi, and H. Kawarada, *Jpn. J. Appl. Phys.* 32, L200 (1993)

Par91 S. Park and J. Lee, *J. Appl. Phys.* 69, 2618 (1991)

Pie89 W. Piekarczyk, R. Roy and R. Messier, *J. Crystal Growth* 98, 765 (1989)

Pin93 I. Pinter, A. Tebano, A. Paoletti, and P. Paroli, *Diam. Rel. Mater.* 3, 126 (1993)

Ral95 V. G. Ralchenko, E. D. Obraztsova, K. G. Korotushenko, A. A. Smolin, S. M. Pimenov, and V. G. Pereverzev, MRS Symp. Proc. Vol. 383, 153 (1995)

Ram92 R. Ramesham and T. Roppel, *J. Mater. Res.* 5, 1144 (1992)

Rat95 D. Rats, L. Bimbault, L. Vandenbulcke, R. Herbin, and K. F. Badawi, *J. Appl. Phys.* 78, 4994 (1995)

Ree93 S. W. Reeve, W. A. Weimer and F. M. Cerio, *J. Appl. Phys.* 74, 7521 (1993)

Rei95 P. Reinke, P. Kania, and P. Oelhafen, *Thin Solid Films* 270, 124 (1995)

Rud92 R. A. Rudder, G. C. Hudson, J. B. Posthill, R. E. Thomas, R. C. Hendry, D. P. Malta, R. J. Markunas,

T. P. Humphreys and R. J. Nemanich, *Appl. Phys. Lett.* 60, 329 (1992)

Sap94 G. V. Saparin, *Diam. Rel. Mater.* 3, 1337 (1994)

Sha96 T. Sharda, D. S. Misra, D. K. Avasthi, and G. K. Mehta, *Solid State Communications* 98, 879 (1996)

Shi92a Y. Shimada, N. Mutsukura and Y. Machi, *Jpn. J. Appl. Phys.* 31, 1958 (1992)

Shi92b Y. H. Shing, F. S. Pool, and D. H. Rich, *Thin Solid Films* 212, 150 (1992)

Shr90 R. E. Shroder, R. J. Nemanich and J. T. Glass, *Phys. Rev. B* 41, 3738 (1990)

Sin92 R. K. Singh, D. Gilbert, R. Tellshow, P. H. Holloway, R. Ochoa, J. H. Simmons, and R. Koba, *Appl. Phys. Lett.* 61, 2863 (1992)

Sin96a R. K. Singh, D. R. Gilbert, and J. Laveigne, *Appl. Phys. Lett.* 69, 2181 (1996)

Sin96b R. K. Singh, D. R. Gilbert, J. Fitz-Gerald, S. Harkness, and D. G. Lee, *Science* 272, 396 (1996)

Spe94a K. E. Spear and M. Frenklach, in *Synthetic Diamond: Emerging CVD Science and Technology*, K. E. Spear and J. P. Dismukes Eds., John Wiley and Sons, Inc., Pennington, New Jersey, 278 (1994)

Spe94b K. E. Spear and M. Frenklach, in *Synthetic Diamond: Emerging CVD Science and Technology*, K. E. Spear and J. P. Dismukes Eds., John Wiley and Sons, Inc., Pennington, New Jersey, 269 (1994)

Ste94 S. S. Staehle, *The Role of the Surface Chemistry of Colloidal Diamond in the Processing of Diamond Coatings*, Masters Thesis, Department of Materials Science and Engineering, University of Florida 1994

Sti96 J. Stiegler, Y. von Kaenel, M. Cans, and E. Blank, *J. Mater. Res.* 11, 716 (1996)

Sto93 B. R. Stoner, C. Kao, K. M. Malta, and R. C.

Glass, *Appl. Phys. Lett.* 62, 2347 (1993)

Sto94 L. St-Onge and M. Moisan, *Plasma Chem. Proc.* 14, 87 (1994)

Tel95 R. Tellshow, *Chemical Vapor Deposition of Diamond Coatings on Ferrous Substrates Via Interlayer Technology*, Masters Thesis, Department of Materials Science and Engineering, University of Florida 1995

Val91 J. L. Valdes, J. W. Mitchel, J. A. Mucha, L. Seibles, and H. Huggins, *J. Electrochem. Soc.* 138, 635 (1991)

Van67 A. van der Drift, *Philips Res. Reports* 22, 267 (1967)

Wan92 W. Wanlu, L. Kejun, G. Jinying, and L. Aimin, *Thin Solid Films* 215, 174 (1992)

Wat88 I. Watanabe and K. Sugata, *Jpn. J. Appl. Phys.* 27, 1397 (1988)

Wat92 I. Watanabe, T. Matsushita and K. Sasahara, *Jpn. J. Appl. Phys.* 31, 1428 (1992)

Wei90 J. Wei, H. Kawarada, J. Suzuki, and A. Hiraki, *Jpn. J. Appl. Phys.* 29, L1483 (1990)

Wei92 P. S. Weiner, S. Prawer, A. Hoffman, R. R. Manory, P. J. K. Paterson and S. Stuart, *J. Appl. Phys.* 72, 4643 (1992)

Wil93 C. Wild, P. Koidl, W. Müller-Sebert, H. Walcher, R. Kohl, N. Herres, R. Locher, R. Samlenski, and R. Brenn, *Diam. Rel. Mater.* 2, 158 (1993)

Xil94 P. XiLing and G. ZhaoPing, *Thin Solid Films* 239, 47 (1994)

Yan94 P. C. Yang, W. Zhu, and J. T. Glass, *J. Mater. Res.* 9, 1063 (1994)

Yan95 G. S. Yang, M. Aslam, K. P. Kuo, D. K. Reinhard, and J. Asmussen, *J. Vac. Sci. Technol. B* 13, 1030 (1995)

Yan96	W. S. Yang, J. H. Je, *J. Mater. Res.* 11, 1787 (1996)
Yar95	T. Yara, H. Makita, A. Hatta, T. Ito, and A. Hiraki, *Jpn. J. Appl. Phys.* 34, L312 (1995)
You93	D. L. Youchison, C. R. Eddy, Jr., and B. D. Sartwell, *J. Vac. Sci. Technol. A* 11, 103 (1993)
Yug91	S. Yugo, T. Kanai, T. Kimura, and T. Muto, *Appl. Phys. Lett.* 58, 1036 (1991)

BIOGRAPHICAL SKETCH

Donald Russell Gilbert was born in Framingham, Massachusetts on September 20, 1967. He graduated from Framingham North High School in 1986. He went on to attend Rensselaer Polytechnic Institute, where he received a Bachelor's of Science degree (magna cum laude) in Physics in May of 1990. Following his graduation, he spent a brief period working part-time for LMA, Inc., where he was introduced to laboratory research and the chemical vapor deposition process of diamond formation. As a result of this experience, he applied to and was enrolled in the graduate program of the department of Materials Science and Engineering at the University of Florida, to further pursue research in diamond CVD towards his Ph.D. degree.

I certify that I have read this study and that in my opinion it conforms to acceptable standards of scholarly presentation and is fully adequate, in scope and quality, as a dissertation for the degree of Doctor of Philosophy.

Raj K. S

Rajiv K. Singh, Chair
Professor of Materials
Science and Engineering

I certify that I have read this study and that in my opinion it conforms to acceptable standards of scholarly presentation and is fully adequate, in scope and quality, as a dissertation for the degree of Doctor of Philosophy.

CR Abernathy

Cammy R. Abernathy
Professor of Materials
Science and Engineering

I certify that I have read this study and that in my opinion it conforms to acceptable standards of scholarly presentation and is fully adequate, in scope and quality, as a dissertation for the degree of Doctor of Philosophy.

Paul H Holloway

Paul H. Holloway
Professor of Materials
Science and Engineering

I certify that I have read this study and that in my opinion it conforms to acceptable standards of scholarly presentation and is fully adequate, in scope and quality, as a dissertation for the degree of Doctor of Philosophy.

Robert T. DeHoff

Robert T. DeHoff
Professor of Materials
Science and Engineering

I certify that I have read this study and that in my opinion it conforms to acceptable standards of scholarly presentation and is fully adequate, in scope and quality, as a dissertation for the degree of Doctor of Philosophy.

D. O. Shah

Dinesh O. Shah
Professor of Chemical
Engineering

This dissertation was submitted to the Graduate Faculty of the College of Engineering and to the Graduate School and was accepted as partial fulfillment of the requirements for the degree of Doctor of Philosophy.

August, 1998

Winfred M. Phillips
Dean, College of Engineering

Karen A. Holbrook
Dean, Graduate School